LAWRENCE
LIVERMORE
NATIONAL
LABORATORY

LLNL-TR-643519

Modeled Neutron Induced Nuclear Reaction Cross Sections for Radiochemsitry in the region of Thulium, Lutetium, and Tantalum I. Results of Built in Spherical Symmetry in a Deformed Region

R. D. Hoffman

September 6, 2013

Disclaimer

This work performed under the auspices of the U.S. Department of Energy by Lawrence Livermore National Laboratory under Contract DE-AC52-07NA27344.

LLNL-TR-643519

Modeled Neutron Induced Nuclear Reaction Cross Sections for Radiochemistry in the region of Thulium, Lutetium and Tantalum I. Results of Built in Spherical Symmetry in a Deformed Region

R.D. Hoffman
Computational Nuclear Physics Group
Physics and Life Sciences Directorate
Lawrence Livermore National Laboratory
Livermore, CA 94550
rdhoffman@llnl.gov

February 27, 2015

ABSTRACT

We have developed a set of modeled nuclear reaction cross sections for use in radiochemical diagnostics. Systematics for the input parameters required by the Hauser-Feshbach statistical model were developed and used to calculate neutron induced nuclear reaction cross sections for targets ranging from Terbium ($Z = 65$) to Rhenium ($Z = 75$). Of particular interest are the cross sections on Tm, Lu, and Ta including reactions on isomeric targets.

Subject headings: Nuclear cross sections, Radiochemistry, Nuclear Physics

1. Introduction

1.1. Radiochemistry

Various aspects of nuclear explosive device performance can be determined through the use of radiochemistry. During the UGT (Under Ground Test) Program, select naturally occurring elements were often loaded into a device prior to a test and their activation products subsequently retrieved for counting. The products are measured as isotopic ratios (such as $^{87}Y/^{88}Y$ produced from a stable isotope of the naturally occurring element). From the measured activity and prior knowledge of the amount of loaded detector material, performance aspects could be inferred by comparing the measured isotope ratios with those calculated using particle fluences from one of the design codes and group-averaged cross section sets that have been prepared for this purpose.

This paper continues the collaborative effort between AX-Division (WCI) and N-Section (PLS) to update and improve the existing RADCHEM cross section detector sets. Previous papers treated the regions of bromine and krypton (Hoffman *et al.* 2004a), iodine and xenon (Hoffman *et al.* 2004b), samarium, europium, and gadolinium (Hoffman *et al.* 2004c), scandium, titanium, vanadium, chromium, manganese, and iron (Kelley *et al.* 2005), arsenic (Kelley *et al.* 2006a), nickel, copper, and zinc (Kelley *et al.* 2006b), yttrium, zirconium, niobium, and molybdenum (Hoffman *et al.* 2006c), and iridium and gold (Hoffman *et al.* 2008) Here we focus on thulium, lutetium, and tantalum.

Contents

List of Figures

List of Tables

1.2. Current Detector Sets

Over the last 40 years a number of detector sets have been developed at LLNL and LANL. Twenty-three neutron threshold detector sets and five charged particle sets are currently available. The sets of interest in this modeling effort are as follows:

- Thulium neutron-induced set (Tm0193), used to calculate the production of the ground states of ^{167}Tm ($t_{1/2}$ = 9.25 d), ^{168}Tm ($t_{1/2}$ = 93.1 d), and ^{170}Tm ($t_{1/2}$ = 128.6 d) from stable ^{169}Tm.

- Lutetium neutron-induced set (Lu0284), used to calculate the production of ^{171}Lu ($t_{1/2}$ = 8.24 d), ^{172}Lu ($t_{1/2}$ = 6.70 d), ^{173}Lu ($t_{1/2}$ = 500.4 d), ^{174g}Lu ($t_{1/2}$ = 1209 d), ^{174m}Lu ($t_{1/2}$ = 142.0 d), and ^{177g}Lu ($t_{1/2}$ = 6.65 y) from stable ^{175}Lu and ^{176}Lu. Note that the decay half-lives for ^{173}Lu and ^{174g}Lu have both decreased (by 6% and 3% respectively) from their previous values (Nethaway 1998).

- Tantalum neutron-induced set (Ta0784) ^{182}Ta ($t_{1/2}$ = 114.43 d), and ^{183}Ta ($t_{1/2}$ = 5.1 d) from stable ^{180}Ta and ^{181}Ta.

The cross sections available in these detector sets are summarized in table 1 in appendix A. Most of the cross sections are taken from calculations performed at LLNL and LANL between 1985 and 1993 (Nethaway 1998). The Thulium set includes (n,2n), (n,3n), and (n,γ) reactions on ground states even though each species of interest has a long-lived isomer. Other than reactions on the loaded target ^{169}Tm, which are based on evaluated data, all other cross sections are from a set developed at LANL in 1973 (for an updated evaluation see (Chadwick et. al. 2007). For the lutetium set, all cross sections were initially calculated in 1975. The (n,2n) and (n,γ) cross sections on loaded ^{175}Lu are in agreement with experimental data to a few percent. The ^{173}Lu(n,2n)^{172}Lu cross section is within 1% of its measured value of 2.05 b at 14.8 MeV. The cross sections in the tantalum set are all drawn from the ACTL library (ACTL 1978). All three of these sets can be accessed on the world wide web at http://nuclear.llnl.gov/CNP/nads/main.html.

1.3. Motivation for Updating the Detector Sets

Many of the RADCHEM detector sets updated in our previous modeling efforts had a clear need for improvement. The historical cross section sets do not include charged particles in the exit channel of the neutron-induced reactions. Here, because these targets have such a high Z value, charged particles are strongly inhibited by the Coulomb barrier in the exit channel, so the dominant reactions will only involve neutrons and photons.

Another motivation is drawn from the general improvement in cross section modeling capabilities. In the nearly two decades since these sets were developed, many new cross section measurements have been performed, and the amount of nuclear structure data used to constrain model parameters has increased. Additionally, several efforts have been made to develop consistent approaches to modeling nuclear reaction cross sections (Belgya *et al.* 2005), and there are more accurate methods of calculating and estimating cross sections for which we have no data.

Thirdly, our proposed new evaluation of these cross sections includes an in-depth investigation into the sensitivity of the modeled cross sections to variations in the various statistical model inputs. In doing so we are able to determine which parameters are the most important for a given reaction. This also allows us to estimate how much a calculated cross section will change if new experimental measurements place more constraints on the model inputs.

1.4. Proposed Detector Sets

We consider as targets each of the isotopes listed in Table 1 of Appendix A. For each of these targets, we model the reaction channels indicated in the table. In cases where the residual nucleus has a long-lived isomer (which we define as $t_{1/2} > 1$ μs), we model individual cross sections leading to the ground and isomeric states, as well as an "activation" cross section, defined as the total cross section producing a given isotope. This modeling effort includes all of the reactions previously available in the RADCHEM detector sets, but also includes many additional targets and reaction channels. These additional reactions are included primarily to provide further comparisons to measured cross section data and bolster our confidence in the accuracy of cross sections modeled for unstable targets. These reactions also account for the various possible destruction reactions that

are significant in this mass range.

Our goal is to develop a consistent set that reproduces, as closely as possible, measured cross sections on targets in the *local region of interest*. To do this we develop *local systematics* for the many input quantities used in the theoretical reaction modeling calculations. These systematics are based on experimental data that are often only available for compound nuclear systems formed from a stable target plus a neutron. Of course, we use experimental data whenever it is available, but reactions proceeding through unstable systems are unavoidable in radiochemistry. Short of developing new experimental techniques to measure cross sections on unstable targets, our only hope of reproducing measured activity from UGT shots, and addressing the uncertainty associated with the nuclear cross sections, is to develop cross section sets that reproduce well the measured cross sections in the local region of interest.

In §2 we describe the theoretical techniques used in the modeling effort. §3 describes the input parameters. §4 gives results. We conclude with §5.

2. Nuclear Reaction Theory

2.1. Reaction Mechanisms

Conceptually, we consider nuclear reaction mechanisms to be of two general types: direct processes and compound processes. Direct processes can be pictured as simple interactions of the incident particle with the nuclear potential of the target nucleus. They proceed on a rapid time scale (of order $\sim 10^{-22}$ s), and the reaction products are often highly peaked in the incident particle direction. Direct reactions are generally quite small over the energy range of interest in this study, and have not been included in our calculations.

Compound processes are pictured as complicated interactions proceeding over a much longer timescale ($10^{-15} - 10^{-18}$ s) in which the reaction is mediated by the formation of a "compound nucleus", with the excitation energy of the incident particle being statistically "shared" with the ensemble of nucleons in the target over all energetically allowed degrees of freedom. The reaction products are largely isotropic.

Other intermediate reaction mechanisms exist between these two extremes. We refer to these as "pre-equilibrium" nuclear processes, where a particle may be emitted from the target+projectile compound system prior to equilibration. Over the energy range of interest to this project (a few keV to 20 MeV) we will consider pre-equilibrium and compound nuclear processes, with the pre-equilibrium processes operating principally above 10 MeV of incident particle energy.

2.2. Hauser-Feshbach Statistical Model

A traditional theoretical approach to compound nuclear reactions is the statistical or Hauser-Feshbach model (Hauser & Feshbach 1952). This model is valid for high level densities in the compound nucleus, allowing one to use energy averaged transmission coefficients T, which describe absorption via an imaginary part in the (optical) nucleon-nucleus potential (Mahaux & Weidenmüller 1979). For the reaction I (in state μ) $+j \rightarrow k +$ L (in state ν), with $\mathrm{I}^{\mu} + j$ interacting with center-of-mass energy E_j^{μ} (in MeV), the average cross section is given by

$$\sigma_{jk}^{\mu\nu}(E_j^{\mu}) = \frac{\pi \lambda\!\!\!^{-2}_j}{g_I^{\mu} g_j} \sum_{J,\pi} g_J \frac{T_j^{\mu}(J^{\pi}) T_k^{\nu}(J^{\pi})}{T_{tot}(J^{\pi})} W(J^{\pi}) \tag{1}$$

where the summation extends over all compound nuclear spins and parities J^{π}, μ and ν enumerate states in the target and product (=0 for the ground state, 1 for the 1^{st} excited state, etc.). The cross section has units of area, described by $\pi \lambda\!\!\!^{-2}_j = 0.6566(\hat{A}_j E_j^{\mu})^{-1}$ barns, with $\hat{A}_j = (A_I A_j)/(A_I + A_j)$ being the reduced mass in atomic mass units and E_j^{μ} is the center of mass energy in units of MeV. $\lambda\!\!\!^{-}_j$ is the wavelength related to the wave number k_j in the target plus incident particle channel by $\lambda\!\!\!^{-}_j = 1/k_j$ The statistical weights are given by $g_y^x = (2J_y^x + 1)$. Items without superscripts refer to the compound nucleus.

The transmission coefficients in the numerator are given by $T_j^{\mu}(J^{\pi}) =$ the total transmission coefficient for forming the state J^{π} in the compound nucleus $I^{\mu} + j$ at energy E_j^{μ}. Likewise, $T_k^{\nu}(J^{\pi})$ is the same as $T_j^{\mu}(J^{\pi})$ but for the pair $L^{\nu} + k$ at energy E_k^{ν}. Implicit in these definitions is a sum over all possible $l-$waves and channel spins, i.e.

$$T_j^{\mu}(J^{\pi}) = \sum_{l,s} T_j^{\mu}(J^{\pi}, l, s) \tag{2}$$

where l is any partial wave number (orbital angular momentum) that can couple the state μ to the compound nuclear state having spin and parity J^{π} subject to quantum mechanical selection rules and s is the vector sum of the spins J_I^{μ} and J_j. Hence s

takes on all integer (or half-integer) numbers from $|J_I^\mu - J_j|$ to $J_I^\mu + J_j$.

T_{tot} represents the sum of transmission coefficients over all possible decay channels (i.e. for all particles and photons). The cross section for the formation of species L, regardless of its state ν, is obtained by summing Eq. [1] over all bound states ν of L for which the reaction is energetically allowed.

When evaluating these sums, if energies become of interest which exceed the highest discrete excited state for which energy, spin, and parity are explicitly known, a nuclear level density formula must be employed. Specifically, the definitions for the transmission coefficients $T_j(J^\pi)$, $T_k(J^\pi)$, and $T_{tot}(J^\pi)$ must be modified:

$$T_k(J^\pi) = \sum_{\nu=0}^{\omega} T_k^\nu(J^\pi) + \sum_{J^\nu \pi^\nu} \int_{\xi_L^\omega}^{\xi_L^{max}} T_k^\nu(\xi_L^\nu, J^\pi) \rho(\xi_L^\nu, J^\nu, \pi^\nu) d\xi_L^\nu d\pi^\nu dJ^\nu \quad (3)$$

where for the nucleus L, ξ_L^ω is the energy of the highest excited state, ω, of known energy, spin, and parity; $\xi_L^{max} = E_k^0 = E_j^0 + Q_{jk}$ is the maximum excitation energy available, and $\rho(\xi_L^\nu, J^\nu, \pi^\nu)$ is the density of states per unit energy of spin and parity J^ν and π^ν at the excitation energy ξ_L^ν. The above integral approximates a sum and is subject to the same quantum mechanical restrictions implied in the definition of the transmission function.

2.3. Width Fluctuations

In addition to the ingredients required for Eq. [1], we apply width fluctuation corrections ($W(J^\pi)$, hereafter WFC), which define correlation factors with which all partial channels of incoming particle j and outgoing particle k, passing through excited state (E, J, π), should be multiplied. The major effect is to enhance the elastic channel and accordingly decrease the other open channels. They are most often observed at or near channel opening energies, for example when a (p,γ) and a (p,n) channel compete and the weaker (p,γ) channel is enhanced. Above a few MeV of excitation energy, when many competing channels are open, WFC's can be neglected.

A reasonably complete treatment for the WFC, obtained with the Gaussian orthogonal ensemble (GOE) approach, requires the evaluation of a triple integral and to date has been considered much to costly to apply in nuclear cross section calculations. Several approximations have been developed, the most popular ones are the Moldauer model (Moldauer 1976), and the HRTW model (Hofmann *et al.* 1975). We use the Moldauer model approximation in this study. For a detailed description of the full (GOE) treatment and a comparison with the Moldauer and HRTW approximation models mentioned above, see (Hilaire Lagrange & Koning 2003).

2.4. Pre-Equilibrium Processes

For excitation energies starting around 10 MeV, pre-equilibrium processes become important. The pre-equilibrium cross section is subtracted from the total reaction cross section leading to the first compound nucleus, and is usually unimportant for subsequent compound nuclei. Here we describe equilibration of the compound nuclear system in terms of the exciton model (Cline & Blann 1971) including alpha particle emission (Milazzo-Colli & Braga-Marcazzan 1973). We adopt an initial 2-particle 1-hole configuration. Average rates for internal transitions, corrected for the Pauli principle by (Cline 1972), are related by the formulas of (Williams 1970) to the absolute square of the average effective matrix element $|M|$ of the residual interactions as per Eq. [7] of (6). The dependence of $|M|^2$ on mass number and excitation energy is

$$|M|^2 = \langle FM \rangle A^{-3} E^{-1} \quad (4)$$

The description of alpha particle emission in the pre-equilibrium model is a straightforward extension of nucleon emission, assuming nucleons preform alpha clusters. In making such an extension, one introduces a parameter ϕ which represents the probability that the incoming particle will strike a pre-formed alpha cluster.

In the pre-equilibrium stage of the reaction, particle emission is assumed to be the only decay mode. For the equilibration, the WFC corrected Hauser Feshbach formula (Eq. [1]) is applied. All subsequent processes are treated as sequential evaporation steps.

2.5. The TALYS Hauser-Feshbach Reaction Code

We model our cross sections using the statistical model code TALYS (6), which embodies all of the physical models discussed above. The version of the code we use is TALYS-1.4, available from the TALYS web site. We have made several mod-

ifications, primarily to the level density routines. Prior versions of the code were used to develop parts of the existing RADCHEM data sets.

In the following we discuss the important ingredients of statistical model calculations, and the methods utilized to estimate them. These are the requisite nuclear structure data, such as the binding energies of all nuclei included (which define the separation and reaction threshold energies and Q-values of the various reaction channels considered), as well as the energies, spins, and parities of the ground states and all known excited states of these nuclei, and the detailed branching ratios for the gamma-ray cascade from excited to low-lying states. Also needed are parameters controlling the width fluctuation corrections and the pre-equilibrium model, the particle and γ-transmission coefficients, and the nuclear level densities of all nuclei involved in a given reaction. The reliability with which these ingredients can be calculated determines the accuracy (or reliability) of a given cross section calculation.

3. Inputs to the Hauser-Feshbach Model

3.1. Nuclear Structure Data

3.1.1. Nuclear Masses and J^π Assignments

We adopt for nuclear masses the experimental mass excess values located in the "masses" subdirectory in the TALYS-1.4 database Spin and parity assignments for the ground state and isomer targets (Tuli 2000) are given in Table 1 (Appendix A). In Table 2 we provide reaction Q-values for the cross sections modeled in this study.

3.1.2. Nuclear Level Schemes

The nuclear level schemes for the all species are derived from ENDSF and located in the "levels" subdirectory in the TALYS-1.4 structure database. Important quantities for our calculations are the level energies, spin and parity assignments (see Table 3 in Appendix A.3) The number of excited levels adopted for each nucleus is given as the quantity "N" (we always include a ground state, i.e. when N=0 only the ground state is included).

3.2. Transmission Coefficients

3.2.1. Transmission Coefficients for Particles

Our modeling effort includes reactions with incident neutrons. To accurately calculate the exit

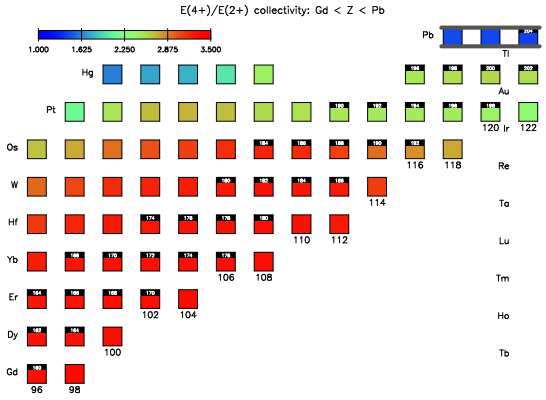

Fig. 1.— Collectivity (the ratio of energies of the first 4+ and 2+ levels in even-Z even-N nuclei) in the region from Gadolinium to Lead. The scale gives the ratio E(4+)/E(2+), 1.0 (blue) is spherical, 2.3 (green) transitional, and ≥ 3 (red) is strongly deformed.

channel cross sections we also include transmission coefficients for protons, alpha-particles, and deuterons. For neutrons and protons, we develop our own optical model for deformed rare-earth nuclei. For alphas and deuterons, we adopt well established spherical optical models (see below).

3.2.2. Considerations Regarding Collectivity and Nuclear Deformations

Our region of interest extends from $98 \leq N \leq 112$. To gauge the onset of collective effects we appeal to nuclear systematics. One such measure of "collectivity" is the ratio vs. neutron number N of the energy of the first $J^\pi = 4^+$ excited state to the first $J^\pi = 2^+$ excited state in even-Z even-N nuclei (Figure 1). Spherical (magic closed shell) nuclei exhibit collectivity near 1.6 and are clearly seen in the Z=82 (Pb) closed proton shell. Deformed vibrators occur between 2.0 - 2.4 (all the nuclei of Hg and Pt for $108 \leq$ N ≤ 122), followed by transitional nuclei up to 3.3 (W and Os), where a true rotational character is evident. The loaded ^{169}Tm, ^{175,176}Lu, and ^{180,181}Ta targets sit firmly in the zone of strong deformation. This suggests we should adopt a deformed optical model for all our calculations, assuming a a rotational character for all nuclei with $Z \leq 77$. We adopt the deformation parameters (β) from the FDRM calculation of (Möller *et al.* 1995).

3.2.3. *The Neutron and Proton Optical Potential*

The optical potential used in determining the neutron and proton transmission coefficients (FDOM) was developed by F. Dietrich (Dietrich 2001). It is a deformed potential with a standard Woods-Saxon shape. The real volume potential has a depth of

$$\begin{aligned} V_{vol.}(E) &= (50.125 - 0.2331E) \\ &- \eta_p\eta_t(20.050 - 0.0933E) \\ &+ \xi\frac{0.3Z}{A^{1/3}} \end{aligned} \quad (5)$$

where

$$\eta_t = \frac{A-2Z}{A} \quad (6)$$

and $\eta_p = 1$ for incident neutrons and $\eta_p = -1$ for incident protons. Additionally, $\xi = 1$ for incident neutrons and $\xi = 0$ for incident protons.The real volume potential has a mean radius and diffusivity of $r_{vol.} = 1.25A^{1/3}$ and $a_{vol.} = 0.65$ fm, respectively.

The imaginary volume potential has a depth of

$$\begin{aligned} W_{vol.}(E) &= (-1.357 + 0.1696E) \\ &- \eta_p\eta_t(-0.543 + 0.0678E) \end{aligned} \quad (7)$$

When $W_{vol.} < 0$, it is set to zero (i.e. we do not allow $W_{vol.}$ to become negative). The mean radius and diffusivity are the same as for the real volume potential.

The imaginary surface potential is broken into two parts. For incident energies less than 8 MeV, it has the form

$$\begin{aligned} W_{surf.}(E) &= (3.743 + 0.334E) \\ &- \eta_p\eta_t(1.497 + 0.134E) \end{aligned} \quad (8)$$

Above 8 MeV, we use

$$\begin{aligned} W_{surf.}(E) &= (6.974 - 0.0697E) \\ &- \eta_p\eta_t(2.790 - 0.0279E) \end{aligned} \quad (9)$$

As with the imaginary volume, we only use positive values for the surface potential, replacing negative values with zero. The mean radius is the same as for the volume terms, but the diffusivity is taken to be $a_{surf.} = 0.58$ fm.

Last of all we include a real spin-orbit potential with a depth of 8.427 MeV with the same mean radius and diffusivity as the volume terms. Additionally, for incident protons, one must include the Coulomb potential.

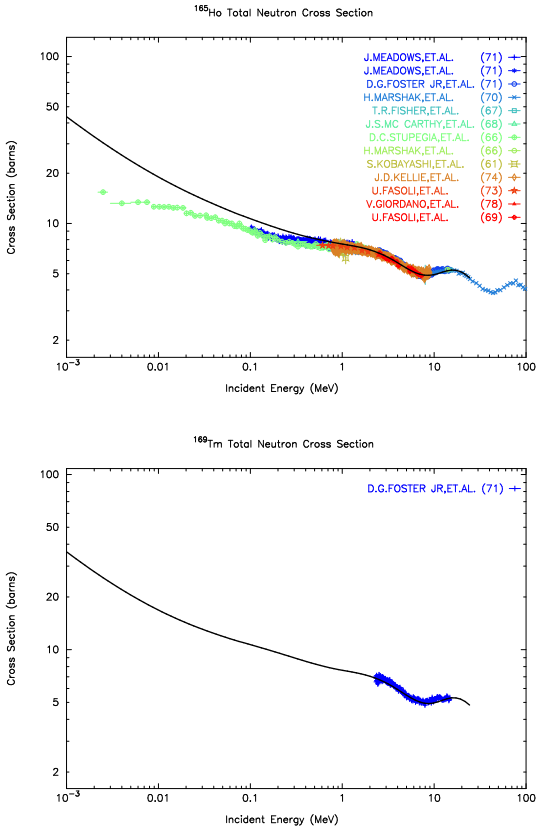

Fig. 2.— Total measured neutron cross sections vs. FDOM Optical Potential for ^{165}Ho+n and ^{169}Tm+n.

The particle transmission coefficients were generated by the optical model code ECIS-95 (Raynal 1996), using a deformed potential. For $Z \leq 77$ we used a rotational model and allow up to quadrupole deformations. We include only one or two excited states. The states used are the ground state and first $J^\pi = 2^+$, 4^+ for even-Z even-N nuclei. For the remaining nuclei, a fictitious 0^+, 2^+, 4^+ level scheme was developed. The energies for the levels were found by averaging the energies of the nearest even-Z even-N nuclei.

3.2.4. *Evaluation of the Neutron and Proton Optical Potential*

We present in Figure 2 results of the optical model compared to measured total neutron cross sections. The comparisons in Figure 2 are for total neutron cross sections on ^{165}Ho and ^{169}Tm. Other experimental total neutron cross section data in this region generally consists of a single point at roughly 14 MeV, or several points be-

low 10 keV of excitation energy. For cases with a single data point near 14 MeV, the optical model closely replicated the experimental data (typically within 10%). No total proton cross section data was available in this region.

The comparison between the calculated total neutron cross sections from our rotational FDOM optical potential and available experimental data indicates a reasonable degree of agreement.

Further information regarding the quality of the neutron optical potential may be obtained by comparing the s- and p-wave strength functions and mean scattering radii predicted by the model to measured values. We make such a comparison in Figure 3. Each of these plots show the ratio of the quantity predicted by the optical potential to the measured value, plotted against the mass of the compound (target plus neutron) system. The error bars reflect this same ratio using the upper and lower errors in the measured values. Hence, if the error bars cross unity, the optical model prediction is within the errors of the measured value. Our interest here is for $185 \leq A \leq 200$. For the s-wave strength functions (S_0), we see that many of the optical model predictions lie within the errors of the measured values. In all cases, the modeled/measured ratio is with a factor of two (indicated by the two outer dotted lines). The predicted p-wave strength functions (S_1), are slightly higher than a factor of two of the measured values. The mean scattering radii predicted by the optical potential (R'), are in very good agreement with the measurements.

3.2.5. The Alpha and Deuteron Optical Potentials

We have included possible alpha and deuteron exit channels (and appropriate transmission coefficients) in this modeling effort. For the alpha particles, we use the optical potential of (Avrigeanu *et al.* 1994), for deuterons we use (Lohr & Haeberli 1974).

We do not include a quality analysis of these potentials in this report. The deuteron and alpha exit channels are, in every case, very small when compared to the dominant channel, accounting for at most 1% of the total reaction cross section. Therefore, any sensitivity to the alpha and deuteron potentials will only be apparent in these weak exit channels which will have little or no impact on the analysis of UGT shots.

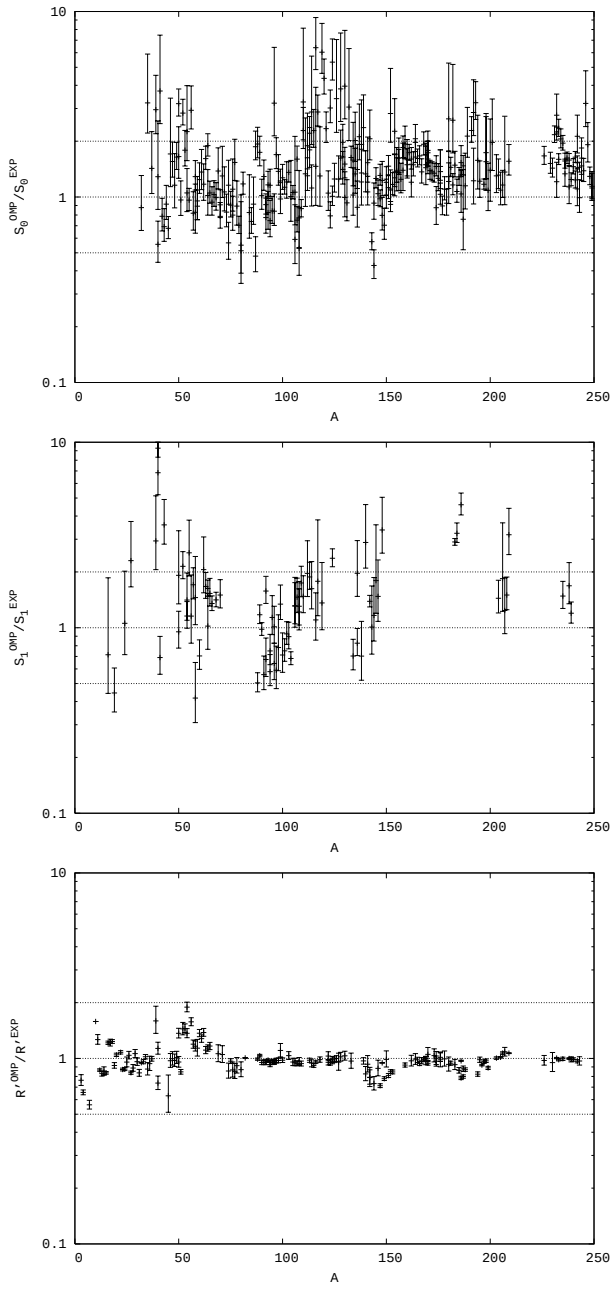

Fig. 3.— Measured s- and p-wave strength functions and mean scattering radii compared to the predictions of the rotational FDOM optical potential. The measured values for the s-wave and p-wave strength functions (S_0 and S_1) are taken from (Belgya *et al.* 2005). Measured scattering radii are taken from (Mughabghab *et al.* 1981). Plotted are the ratios of the modeled quantities to their measured counterparts. The dotted lines indicate unity and factor of two deviations.

3.2.6. Transmission Coefficients for Photons

Gamma ray transmission coefficients were calculated using a simple model which depends only

on the multi-pole type (XL) and the transition energy (ϵ), as encoded in STAPRE. They are related to the gamma ray strength function $f^{\gamma}_{XL}(\epsilon)$ by

$$T^{\gamma}_{XL}(\epsilon) = 2\pi\epsilon^{2L+1} f^{\gamma}_{XL}(\epsilon) \quad (10)$$

The energy dependence of the strength function was determined using the GDR model with enhanced generalized Lorentzian (EGLO) line shapes (Kopecky *et al.* 1993). In particular, the E1 strength function is given by

$$f^{\gamma}_{E1}(\epsilon) = \mathcal{N}\frac{4}{3\pi}\frac{e^2}{\hbar c}\frac{1}{M_p c^2}\times \left[\frac{\epsilon\Gamma_{GDR}(\epsilon,T_f)}{(\epsilon^2-E^2_{GDR})^2+(\Gamma_{GDR}(\epsilon,T_f)\epsilon)^2}+ 0.7\frac{\Gamma_{GDR}(0,T_f)}{\epsilon^3}\right] \quad (11)$$

where M_p is the proton mass. The energy dependent width $\Gamma_{GDR}(\epsilon,T_f)$ is given by

$$\Gamma_{GDR}(\epsilon,T_f) = \left[\kappa+(1-\kappa)\frac{\epsilon-\epsilon}{E_{GDR}-\epsilon}\right]\times \frac{\Gamma_{GDR}}{E^2_{GDR}}\left[\epsilon^2+(2\pi T_f)^2\right] \quad (12)$$

with $\epsilon = 4.5$ MeV. For nuclei with $A < 148$, the factor κ is unity. For heavier nuclei, $\kappa = 1 + 0.009(A-148)^2\exp[-0.18(A-148)]$. The T_f that appears in Equations 11 and 12 is the temperature of the final state, determined from the level density parameters. For a backshifted transition energy $U = S_n - \epsilon - \Delta$, one determines the energy dependent level density parameter (Eq. 26). Provided U is positive, the temperature is given by

$$T_f = \frac{a}{2}\left[1+\sqrt{1+4aU}\right] \quad (13)$$

Otherwise, $T_f = 1/a$.

Experimental values for two GDR resonances are available in this region (Belgya *et al.* 2005). Based on these measurements, we have adopted a systematic description of these parameters for other targets. Using only measured GDR parameters from the local region of interest, we developed the following systematic fits:

$$\begin{aligned} E_1 &= 6.42 + 0.03\times A_C \text{ MeV}\\ \Gamma_1 &= 2.95 - 0.002\times A_C \text{ MeV}\\ \sigma_1 &= -88.09 + 1.77\times A_C \text{ mb}\\ E_2 &= 19.3 - 0.024\times A_C \text{ MeV}\\ \Gamma_2 &= 5.03 - 0.004\times A_C \text{ MeV}\\ \sigma_2 &= -443.0 + 4.29\times A_C \text{ mb} \end{aligned} \quad (14)$$

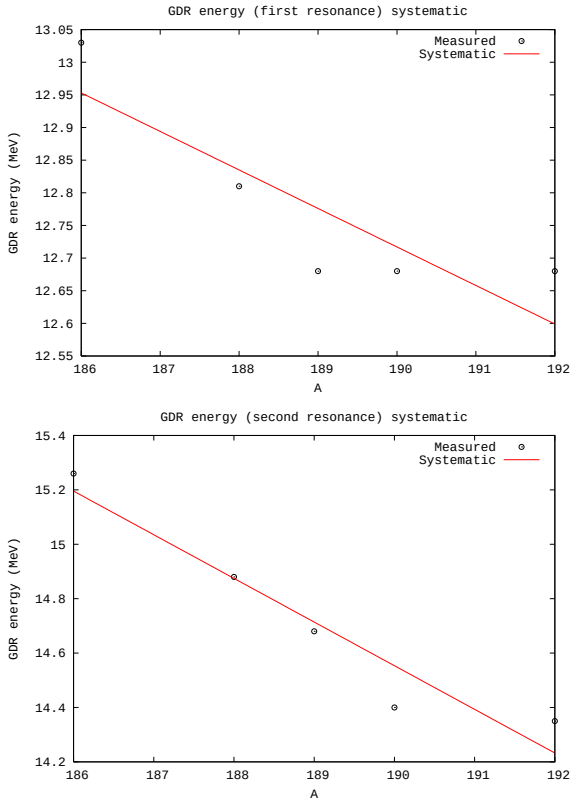

Fig. 4.— Systematics for the GDR energy, first resonance on the top panel, second on the bottom. The measured data in the local region of interest, indicated by black circles, are taken from (Belgya *et al.* 2005).

where A_C is the mass number of the compound nucleus. The resulting systematic fits are presented in Figures (4-6).

We also include M1, E2, M2, E3, and M3 transitions in our modeling. For the M1 strength function, we adopt a Simple Lorentzian (SLO) model

$$f^{\gamma}_{M1}(\epsilon) = \mathcal{N}_{M1}\frac{4}{3\pi}\frac{e^2}{\hbar c}\frac{1}{M_p c^2}\times \frac{\epsilon\Gamma_{GDR}}{(\epsilon^2-E^2_{GDR})^2+(\Gamma_{GDR}\epsilon)^2} \quad (15)$$

with the global set of GDR parameters given in (Belgya *et al.* 2005):

$$\begin{aligned} E_{GDR} &= \frac{41}{A^{1/3}}\\ \Gamma_{GDR} &= 4 \end{aligned} \quad (16)$$

The overall normalization for the M1 strength function ($\mathcal{N}_{M1}$) is determined such that

$$\frac{f_{E1}(S_n)}{f_{M1}(S_n)} = 0.0588\cdot A^{0.878} \quad (17)$$

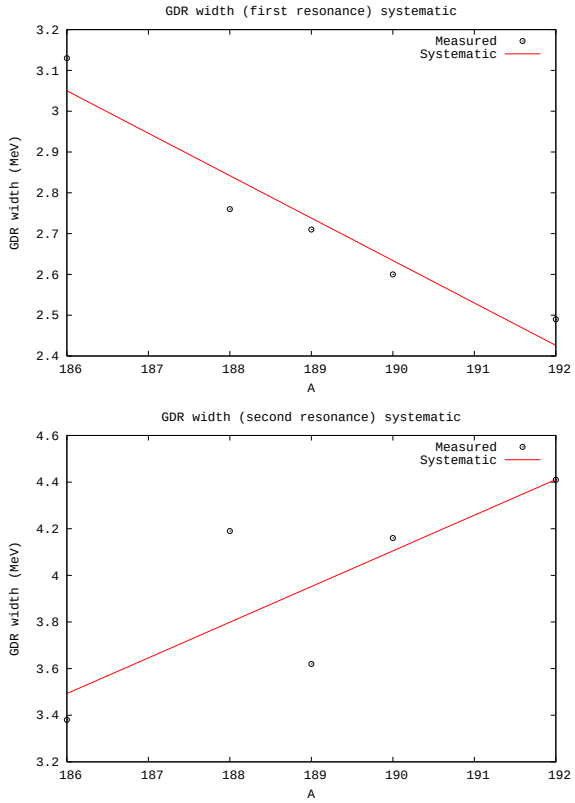

Fig. 5.— Systematics for the GDR width.

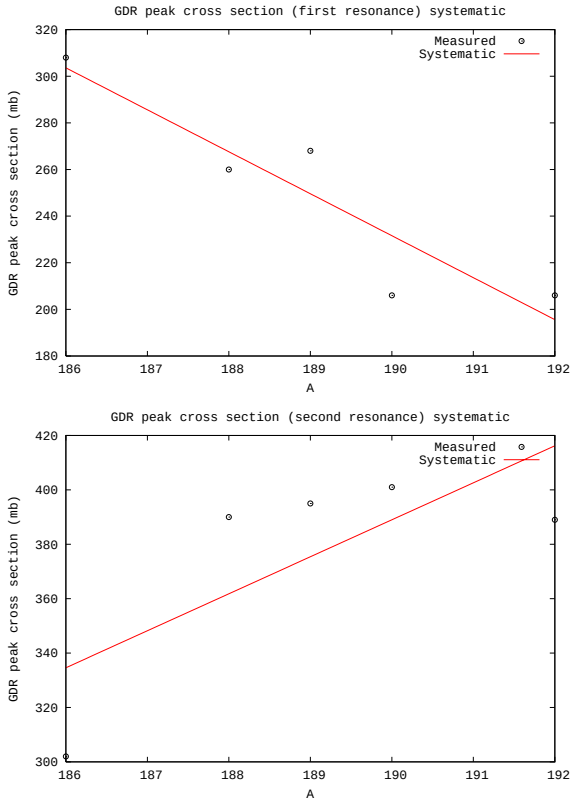

Fig. 6.— Systematics for the GDR peak cross section.

where S_n is the neutron separation energy.

The remaining transmission coefficients are simply proportional to ϵ^{2L+1}, their strength functions are constants. In particular,

$$\begin{aligned} f^{\gamma}_{E2}(\epsilon) &= 7.2\times10^{-7}A_C^{2/3}f^{\gamma}_{E1}(S_n) \\ f^{\gamma}_{M2}(\epsilon) &= 2.2\times10^{-7}f^{\gamma}_{E1}(S_n) \\ f^{\gamma}_{E3}(\epsilon) &= 3.4\times10^{-13}A_C^{4/3}f^{\gamma}_{E1}(S_n) \\ f^{\gamma}_{M3}(\epsilon) &= 1.1\times10^{-13}A_C^{2/3}f^{\gamma}_{E1}(S_n) \end{aligned} \quad (18)$$

where S_n is the neutron separation energy. In all cases, E1 is the dominant multipole.

The factor $\mathcal{N}$ appearing in equation 11 is a normalization constant, determined by fitting the average total s-wave radiation width at the neutron binding energy,

$$\begin{aligned} \langle\Gamma_\gamma\rangle_0 &= \frac{J+1}{2J+1}\left\langle\Gamma_\gamma\left(B_n, J+\frac{1}{2}\right)\right\rangle \\ &+ \frac{J}{2J+1}\left\langle\Gamma_\gamma\left(B_n, J-\frac{1}{2}\right)\right\rangle \end{aligned} \quad (19)$$

$$\Gamma_\gamma\left(E,J\right) = \frac{T_\gamma(E,J)}{2\pi\rho(E,J)}\ (\mathrm{meV})$$

(Uhl & Strohmaier 1976). Here, J is the spin of the target nucleus. The gamma-ray transmission coefficients are evaluated as in Eq. 3 with the summation over multipoles instead of spins and parities.

Since the total s-wave radiation width is generally measured only for stable isotopes plus a neutron, we have developed a systematic approach for estimating this value for the many unstable nuclei in our region of interest.

The systematic we adopt is from Kopecky and is shown in Figure (7). The spline fit is indicated by the red line, the blue and green lines are ±20% variations that we adopt as typical of the average uncertainties given by the grey error bars. The darkened (black) points and their respective errors are for odd-Z compound nuclei. Whenever they are available, we use measured radiation widths instead of systematics to normalize the photon transmission coefficients.

When used to calculate neutron capture (n,γ) cross sections we found that the normalization to the photon-transmission function provided by the $\langle\Gamma_\gamma\rangle_0^{\mathrm{sys}}$ systematic reproduced measured

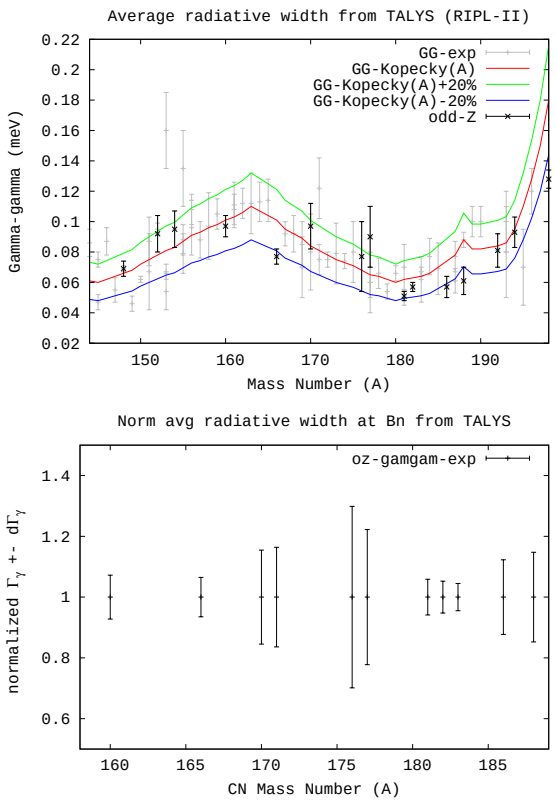

Fig. 7.— Systematics for average total s-wave radiation widths (meV) vs. A for compound nuclei in the range $145 \leq A \leq 200$. The upper figure shows the central systematic (red line) and a $\pm 20\%$ variation above and below it. Black values with error bars are for odd-Z target compound nuclei, the grey values with error bars are for even-Z targets. The lower figure shows the uncertainties normalized to their central values. The systematic is from Kopecky.

Maxwellian Averaged cross sections (MACS) to about a factor of 2. We suspect that the strong deformation in this region is affecting our results through the level densities that are developed with a "built-in" spherical assumption.

3.3. Nuclear Level Densities

3.3.1. Level Density Models

Another important input to the statistical model code, especially for the capture reactions, is the nuclear level density. For this project, we have adopted a standardized, semi-empirical approach (Gilbert & Cameron 1965) which is numerically efficient, can be tied to experimental data, and is fairly accurate. The level density is described by two functions. Both are energy dependent, the second factor contains the spin dependence. This is the "Back-shifted Fermi Gas" formulation of the nuclear level density:

$$\rho\left(U,J\right) = \rho\left(U\right) f\left(U,J\right) \tag{20}$$

where $\rho(U)$ is the state density, with $U = E - \Delta$ the back-shifted energy. Δ is the so called "pairing energy", and J is the spin of the compound nucleus. We will further treat each of these in two ways, depending on the excitation energy of interest. The demarcation point will be roughly between the energy range of the known excited levels of a given compound nucleus (the low energy domain), and near (and above) the neutron binding energy (the high energy domain).

For the high energy domain, we describe the level density assuming a Fermi gas formula,

$$\rho\left(U\right) = \frac{\sqrt{\pi}}{12} \frac{\exp\left(2\sqrt{aU}\right)}{a^{1/4}U^{5/4}} \frac{1}{\sqrt{2\pi}\sigma} \tag{21}$$

$$f\left(U,J\right) = \frac{2J+1}{2\sigma^2} \exp\left[\frac{-\left(J+\frac{1}{2}\right)^2}{2\sigma^2}\right] \tag{22}$$

where $a(E)$ is the level density parameter (in MeV^{-1}). The spin cutoff parameter σ^2 is defined as

$$\sigma^2 = \lambda\sqrt{aU}A^{2/3} \tag{23}$$

The level density assumes an equal distribution of parity states. Note that at low excitation energy (for a positive back-shift), Eq. 21 diverges. At low energies, the nuclear level density is better described by a constant temperature formula:

$$\rho(E) \propto \exp\frac{E - E_0}{T} \tag{24}$$

The level density parameters can be calculated using experimental data. For the Fermi-gas state density (Eq. 21), the level density parameter, $a(E)$, can be related to the average level spacing (D_0) near the neutron binding energy. We provide for odd-Z compound nuclei the average level spacings in figures 8

The pairing energies used in the calculation of the back shifted energy are calculated as differences of binding energies (Bohr & Mottelson). The constant temperature parameters E_0 and T, can be chosen to provide a state density that goes through the low lying spectroscopic levels subject to the choice of a matching energy, E_x, chosen someplace between the high and low energy regions of interest, at which the two state densities

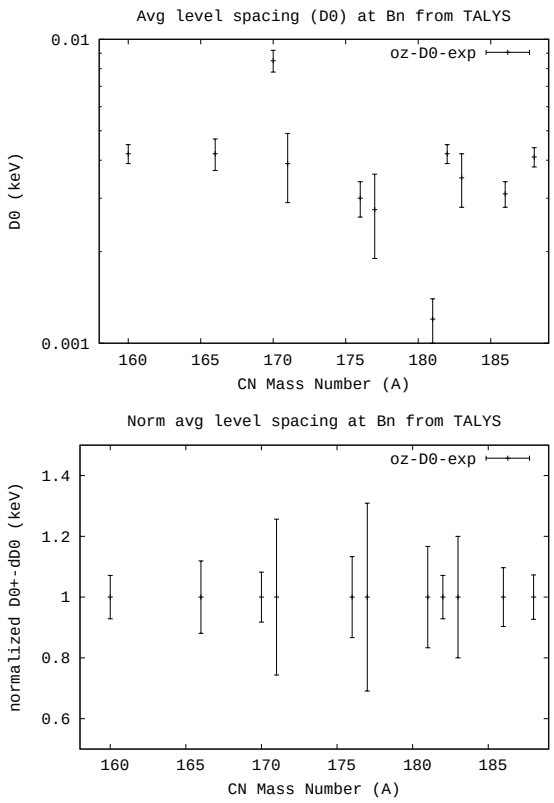

Fig. 8.— Average level spacing (D_0) in keV for odd-Z compound nuclei in our range of interest. Also shown are the uncertainties normalized to the central values. Data from (Belgya *et al.* 2005).

match (point and slope). We describe below how we determined these parameters for all of the nuclei considered in this study.

3.3.2. Level Densities Above the Neutron Binding Energy

Our goal is to fit the level density parameter a in Eq. 21 to experimental data where available. We adopt an energy dependent form, $a(U, Z, N)$, (Iljinov *et al.* 1992), and begin by fixing the spin cutoff parameter and the pairing energies.

The Spin Cutoff Parameter

The spin cutoff parameter σ^2, Eq. 23, characterizes the spin distribution of the Fermi gas level density. It depends on the parameters a, the level density parameter, and λ, which determines the effective moment of inertia for the nucleus in question. In principle it could be determined by experiment, for example, by comparing ratios of cross sections leading to different isomers of the product nucleus (Keisch 1963). Because data like this is often sparse, especially in the limited regions of the periodic chart we are interested in, and because we are often interested in reactions that proceed on or through radioactive species where no such data exists, we must resort to models. In our analysis, we fix $\lambda = 1$ in Eq. 23, corresponding to the moment of inertia of a rigid sphere.

Pairing Energies

In determining the back-shift Δ, also known as the pairing energy, we used a slightly modified version of the method of Rauscher (Rauscher *et al.* 1997). The total pairing energy is equal to the sum of the proton and neutron pairing energies

$$\begin{aligned} \Delta(Z,N) &= \frac{1}{2}\left(\Delta_p + \Delta_n\right) \\ \Delta_p(Z,N) &= E^G(Z,N) \\ &- \frac{1}{2}E^G(Z-1,N) \\ &- \frac{1}{2}E^G(Z+1,N) \\ \Delta_n(Z,N) &= E^G(Z,N) \\ &- \frac{1}{2}E^G(Z,N-1) \\ &- \frac{1}{2}E^G(Z,N+1) \end{aligned} \tag{25}$$

where $E^G(Z,N)$ is the binding energy of the nucleus (Z,N). In calculating the binding energies of the various nuclei, we use the experimental mass excesses listed in the Möller and Nix tables (Möller *et al.* 1995).

The Level Density Parameter

Given Δ and σ^2, the level density parameter $a(U)$ can be related to the average "s"-wave level spacing at the neutron binding energy (D_0) where such quantities are measured. In particular we assume an energy dependent level density parameter

$$a(U) = \tilde{a}\left[1 + \delta W \frac{f(U)}{U}\right] \tag{26}$$

with $f(U) = 1 - \exp(-\gamma U)$ (Iljinov *et al.* 1992). We further assume that $\tilde{a}$ is of the form $\tilde{a} = \alpha A + \beta A^{2/3}$, similar to (Rauscher *et al.* 1997). We adopt the so-called "microscopic correction" from (Möller *et al.* 1995) as our shell corrections, similar to (Rauscher *et al.* 1997), i.e. $\delta W = E_{mic.}$.

Using the relation

$$D_{calc} = \frac{2}{\rho\left(U, J = \frac{1}{2}\right)} \tag{27}$$

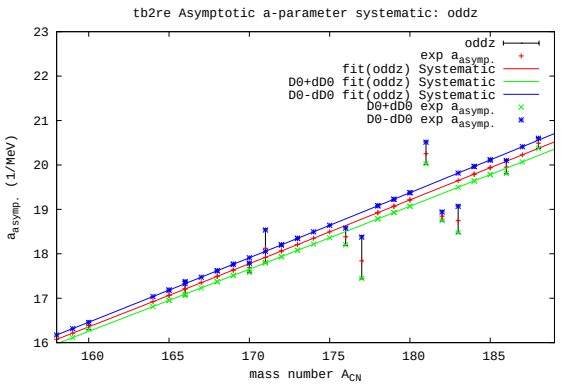

Fig. 9.— Fit to derived "experimental" asymptotic level density parameters, used to systematically determine unknown $\tilde{a}$. The data are obtained from measured s-wave resonance spacing's listed in (Belgya *et al.* 2005), assuming our chosen parameterizations for the shell correction, backshift and spin cutoff parameter. Our systematic, fit only to the data shown in this figure, is represented by the solid red line. The blue and green lines are independent fits to the lower and upper uncertainties on the measured values, respectivley. These fits are only for odd-Z compound nuclei.

for nuclei with spin $s = 0$ and

$$D_{calc} = \frac{2}{\rho\left(U, J = s + \frac{1}{2}\right) + \rho\left(U, J = s - \frac{1}{2}\right)} \tag{28}$$

for nuclei with $s \neq 0$, we numerically solve for the values of α, β, and γ that minimize the quantity

$$\chi^2 = \sum_i \left(\frac{D_0^{\rm calc} - D_0^{\rm exp}}{\delta D_0^{\rm exp}} \right)^2 \tag{29}$$

where $\delta D_0^{\rm exp}$ is the error in the measured D_0 and the sum is taken over measured D_0 for target nuclei in the range $72 \leq Z \leq 79$, $174 \leq A \leq 198$. The resulting fit finds $\alpha = 0.363 \pm 0.002$, $\beta = -1.399 \pm 0.068$, and $\gamma = 0.0577 \pm 6.18 \times 10^{-6}$, and is shown in Figure 9.

3.3.3. Level Densities Below the Neutron Binding Energy

For the lower energy regions, below the neutron binding energy B_n, the nuclear level density has the same formulation as Eq. 20. However, particularly at and below the pairing energy Δ, the state density in Eq. 21 becomes imaginary. Unfortunately, experimental level schemes are rarely known above 2 MeV of excitation energy. In practice we are forced again to assume a model and use all available experimental data to constrain its parameters.

Of course the two prescriptions for the level density must match at some energy intermediate to where they are constrained by experiment. Henceforth we will refer to the high energy level density as ρ_1, and the low energy density as ρ_2.

(Gilbert & Cameron 1965) noticed that the cumulative number of observed levels (the so-called staircase plot, which increase exponentially), can be fit with straight lines in a semi-log plot. They adopted a constant temperature formula to fit these:

$$N(E) = \exp\left[\frac{E - E_0}{T}\right] \tag{30}$$

with $N(E)$ being the cumulative number of levels at excitation energy E, E_0 and T are two free parameters to be fit to the observed level structure. The observable level density is given by

$$\rho_1(E) = \frac{dN(E)}{dE} = \frac{1}{T} \exp\left[\frac{E - E_0}{T}\right] \tag{31}$$

From classical thermodynamics, we have a definition of the nuclear temperature

$$\frac{d}{dE} \log\, \rho_1(E) = \frac{1}{T} \tag{32}$$

where T now takes on the meaning of a nuclear temperature which is constant in the region of the discrete levels. We assume that Eq. 30 can be extrapolated from the region of the known discrete levels to higher energies, where the Fermi-gas level density (ρ_1) is valid. We then define the notion of a fit to the total level density over the entire range as being achieved if: a) a good fit can be made to the low lying levels, b) the observed level spacing at the neutron binding energy is exactly reproduced, and c) the energy of the matching point E_x for the two prescriptions falls between $E = 0$ and $E = B_n$, and that they match at this point with the same slope, i.e. for $E = E_x$:

$$\rho_1(E_x) = \rho_2(E_x) \tag{33}$$

$$\frac{d\log\, \rho_1(E_x)}{dE} = \frac{d\log\, \rho_2(E_x)}{dE} \tag{34}$$

From the first of these, we can determine E_0:

$$E_0 = E_x - T\, \log\, T\rho_2\left(U_x\right) \tag{35}$$

where $U_x = E_x - \Delta$. The second condition can be satisfied by assuming that at E_x the constant nuclear temperature T of the low lying states is

equal to the energy dependent nuclear temperature $\tau(U_x)$ of the high excited states,

$$\frac{1}{T} = \sqrt{\frac{a}{U_x}} - \frac{3}{2U_x} + \frac{(\tilde{a}-a)(1+\gamma U_x)+\tilde{a}\gamma\delta W}{\sqrt{aU_x}} \quad (36)$$

where a is given by Eq. 26. If there is no shell correction, the latter term in the above equation is zero. Typical values for the matching energy are $2 \leq E_x \leq 8$ MeV, and are approximated by $E_x = 2.5 + \frac{150}{A} + \Delta$ (Gilbert & Cameron 1965). The constant temperature fit to the low lying levels of ^{169}Tm which is typical of the fits for all nuclei in this region is presented in Figure 10.

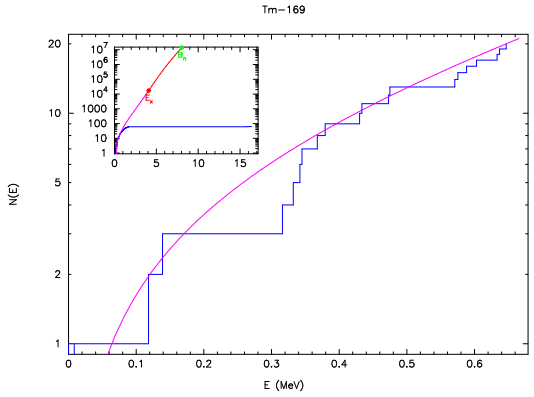

Fig. 10.— Constant temperature level density fits to the low lying spectroscopic levels of ^{169}Tm.

Behavior of the Spin Cutoff Parameter Below E_x

At the matching energy E_x, the spin cutoff parameter is given by Eq. 23. One may define E_{cut} as the energy of the highest known excited level for which energy, spin and parity are explicitly known. We define the following for the behavior of the spin cutoff parameter:

$$\begin{aligned} \sigma_H^2 &= \sigma_{E_x}^2 \\ U_L &= \max\left(E_{cut}-\Delta, 0.1\right) \\ \sigma_L^2 &= \lambda\sqrt{aU_L}A^{2/3} \\ \sigma_G^2 &= \sigma_L^2 + \frac{E-\frac{1}{2}E_{cut}}{E_x-\frac{1}{2}E_{cut}}(\sigma_H^2-\sigma_L^2) \end{aligned} \quad (37)$$

The form σ_G^2 is then used between $\frac{1}{2}E_{cut}$ and E_x. This is the GNASH prescription (Chadwick 1998).

The behavior of σ^2 below E_x will only affect the level density used in Hauser-Feshbach calculations between E_{cut} and E_x, since the discrete levels are accounted for individually. The changes that arise between E_{cut} and E_x are generally small.

The fitted parameters for the total level density are presented in Table A.3. The symbols in the legend are the same as described above. In column five, a "*" indicates the asymptotic level density parameter $\tilde{a}$ was derived from an experimentally known level spacing D_0, otherwise it was derived from the systematic shown in Figure 9.

4. Modeled Cross Sections

4.1. Comparison to Measured Cross Sections

Having developed the various input quantities based on available experimental data in the previous section, we now turn to the results of the STAPRE-H95 model and compare to available measured cross sections in the region of interest. We restrict our attention primarily to ground state targets of ^{169}Tm, ^{175}Lu, and ^{181}Ta (stable loaded detector elements closest in mass to the measured radioactivities). Comparisons to other measured cross sections are provided in the appendices.

4.1.1. Comparison to experimental (n,γ) capture cross sections

In Figure 11 we present comparisons for neutron capture reactions on select targets. Shown is the activation cross section (solid red curve in all plots that follow) defined as the sum of emission (both particle emission and gamma-ray cascade) from the compound nucleus that eventually leads to the ground state of the product (final) nucleus. We also provide the variation in the cross section based on uncertainties in the average radiative width and average level spacing that are used to develop the photon-transimssion coefficient and level density parameter. These cross sections are plotted against the available experimental data, taken from the Experimental Nuclear Reaction Data File (EXFOR 2006).

Our results for ^{169}Tm(n,γ)^{170}Tm are in good agreement considering the amount of scatter that exists in the experimental data. However, we are over-predicting the capture cross sections on both stable Lu and Ta targets. This has been noted in previous evaluation efforts in the Sm-Eu-Gd and Ir-Au regions (Hoffman *et al.* 2004c; Hoffman *et al.* 2008) where strong deformation exists and will be shown over a wider range in the maxwellian averaged cross sections to follow.

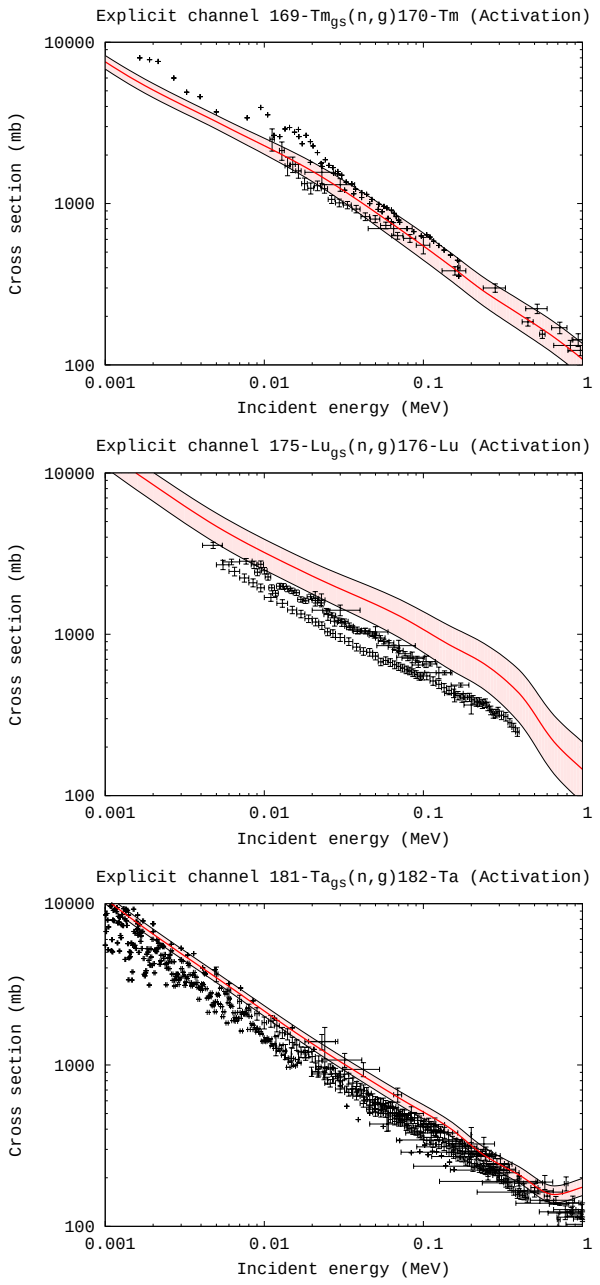

Fig. 11.— Calculated vs. measured (n,γ) cross sections on select stable isotopes in the region of interest. The data is taken from (EXFOR 2006). The red line represents the calculation using the central values of the average radiative width ($\langle\Gamma_\gamma\rangle_0$, Eq. 19) and the measured average level spacing (D_0). The black curves above and below filled with red represent the variation in the cross section when considereing the uncertainties on both quantities (Figures 7 and 9).

Additional comparisons for neutron capture cross sections are presented in Appendix B.1 where a similar degree of agreement between our calculations and experiment is found. The increase in the capture cross section near 14 MeV is a result of the default direct reaction model included in TALYS, while the variation seen for neutron energies $E_n \geq 10$ MeV is due to the amount of pre-equlibrium input to each calculation. The parameter in TALYS that adjusts this is **M2Constant**, with a default value of 1.0 for the choice of pre-equlibrium model we used (an exciton model with analytical transition rates and energy dependent matrix elements, **preeqmode**=1, the default in TALYS). Our variation was 0.75 and 1.25, giving a smaller or larger cross section, respectively. The range of potential values is 0. $\leq$**M2Constant** $\leq$ 100.

4.1.2. Comparison to Maxwellian averaged (n,γ) capture cross sections

Another comparison to experimental data comes from the extensive efforts to measure and evaluate Maxwellian averaged capture cross sections for astrophysical applications (Bao *et al.* 2000). The Maxwellian-averaged neutron capture cross section is defined as the reaction rate $\langle\sigma v\rangle$ divided by the mean velocity $v_T = \sqrt{2kT/\mu}$ at a given temperature T. Here, μ is the reduced mass. For particle fluences and temperatures typical to stellar nucleosynthesis, the velocity distribution of the neutrons is well described by a Maxwell-Boltzmann distribution. In this case, the Maxwellian-averaged cross section reduces to (Beer *et al.* 1992)

$$\frac{\langle\sigma v\rangle}{v_T} = \frac{\int_0^\infty \sigma_{n\gamma} v \Phi(v) dv}{v_T} = \frac{2}{\sqrt{\pi}(kT)^2}\int_0^\infty \sigma_{n\gamma}(E) W(E,kT) dE \quad (38)$$

where $W(E,kT) = E\exp(-E/kT)$ and E is the center of mass energy.

An expanded view of the region of interest is shown in Figure (12), where we provide the 30 keV maxwellian averaged capture cross section for all odd-Z targets for which there is data. Similar plots for even-Z targets are given in Appendix B. On each plot the central calculation is given as a red cross, blue and green stars representing the upper and lower uncertainty in the average radiative widths and level spacings (see Figures 7 and 8) are given above and below the central calculation.

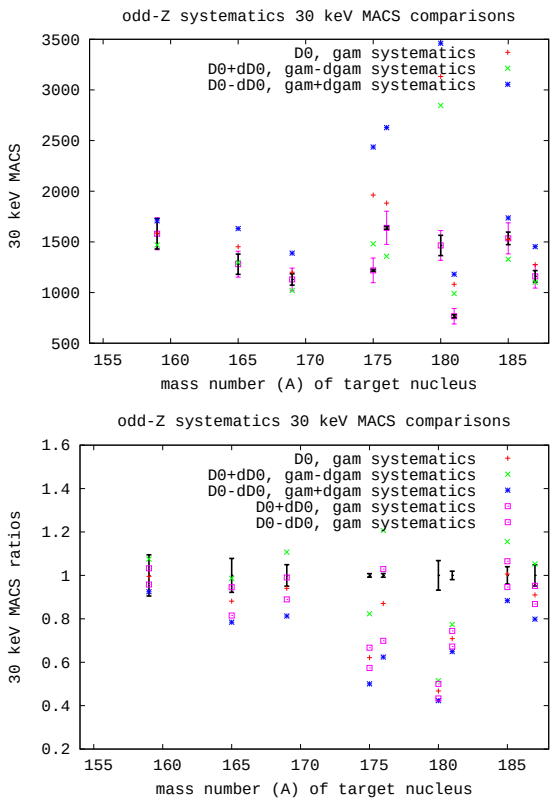

Fig. 12.— 30 keV maxwellian averaged cross sections and their uncertainties (black) for odd-Z species from Tb to Re. The top panel shows the MACS in mb, the bottom panel shows the uncertainties normalized to the central value. Plotted for comparison are three calculated MACS depicting input data to the calculations that reflect the central values (red crosses) and upper and lower uncertainties (blue and green stars) for the average radiative widths and level spacings affecting the photon-transmission coefficients and level densities, respectively

.

The purple squares represent the variation due to uncertainty in the average level spacing alone.

The ability of the statisitcal model to span the range in experimentally measured MACS is very good until one encounters the two targets for Lu and Ta, but then it recovers when the two rhenium isotopes are encountered. The discrepancy is greatest for the ^{180m}Ta case. In each instance of failure, it should be noted that the ground state spins of the target or compound nucleus are high ($J^{\pi} \geq 3$). Our worst cases are those for which both are high, for ^{180m}Ta they are 9- and 7/2+, respectively.

Also shown in Appendix B are our calculated Maxwellian-averaged capture cross sections for ^{169}Tm, ^{175}Lu, and ^{181}Ta, targets to their measured counterparts (Bao *et al.* 2000) over a wide range of neutron energies ($5 \leq E_n \leq 100$ keV). The error bars on all points are identical and represent the measured error for a given cross section at 30 keV. We used spline interpolation to determine the value of the (n,γ) cross section between points on the energy grid. For energies below our lowest grid energy, we assume an (n,γ) cross section with an $E_{lab}^{-1/2}$ dependence. For energies greater than our highest grid energy, we take the cross section to be zero. Only the calculation assuming the central values for the average level spacing and radiation width is shown.

4.1.3. Comparison to experimental (n,2n) cross sections

Our calculated (n,2n) cross sections for select targets are presented in Figure 13 and exhibit very good agreement against measured data for all three targets considered including cross sections to the various final states. Although the loaded Ta isotopes have limited (one or two) experiments reporting activation and ground final state cross sections, each has multiple measurements of the first isomer. The dispersion in the measured data is in some instances large but the various data sets are generally consistent with each other and the range of uncertainty in our input quantities spans the average uncertainty in the measurements for nearly all cases.

Appendix B.2 presents additional comparisons between our modeled (n,2n) cross sections and experiment. Most of the data applies to measurements of cross sections proceeding to ground and first isomer states, which are generally well reproduced by our calculations. The data for activation measurements also agrees well over the limited range (near 14 MeV) that it is often provided For the cases where only ground and isomer data is provided, the sum closely represents the activation cross sections shown (to within 10%).

Interestingly, the variation in the (n,2n) cross sections seen is not due to uncertainties in the average radiative widths or average level spacings used to inform the photon-transmission coefficients or the level density, but rather the amount of pre-equilribrium we included in the model. We chose the value arbitrarily to span the range in measured cross section uncertatinty (roughly 8% near the 14 MeV peak of each

(n,2n) cross section) that exists in nearly all of the experimentally measured cross sections shown in the figures. In past efforts in the regions of Sm-Eu-Gd ((Hoffman *et al.* 2004c)) and Ir-Au ((Hoffman *et al.* 2008)) we used the pre-equilribrium parameter in STAPRE to normalize the peak of the (n,2n) cross sections to the experimental data. Here we did not require an overall normalization (for TALYS we used **M2Constant**=1.0), and a small variation (0.75 ≤**M2Constant** ≤ 1.25) to obtain the variation seen in the plots. These choices had no effect on the capture or (n,n') reactions as the pre-equilribrium treatment does not begin until the (n,2n) separation energy is encountered, by which time the neutron capture cross section is very small.

4.1.4. Comparison to experimental (n,3n) cross sections

Our calculated (n,3n) cross sections for ^{169}Tm, ^{175}Lu and ^{181}Ta are shown in Figure 14. The thresholds for this reaction are above 14 MeV in nearly all cases in this mass range, reflecting the fall off of the (n,2n) reaction channel. Our calculated cross sections are in excellent agreement over the entire range required, although only activation data is available.

4.1.5. Comparison to experimental (n,p) cross sections

For most stable isotopes, the neutron capture and (n,2n) reactions are the dominant neutron induced reaction channels at low and high incident energies, respectively. However, as one moves to the proton rich side of stability, proton separation energies become small, and reaction channels involving charged particles in the exit channel, specifically (n,p), (n,np), and (n,α) can become dominant.

In Appendix B.3 we present our modeled (n,p) cross sections for select target isotopes compared to measurement. In all cases it appears our calculations over-predict the measured cross sections by roughly a factor of three. This behavior is a common feature in our (n,p) cross sections, and is likely due to the simple treatment of pre-equilibrium. Fortunately, the (n,p) cross section is rarely dominant above ∼12 MeV so that errors in our calculation at and above 14 MeV will likely have insignificant impact in network calculations.

Another possibility is the parameterization for our proton optical model. Very little data was available to constrain this so it could be off by up to a factor of three. To check this, one could consult our previous work for ^{197}Au (Hoffman *et al.* 2008), Figure 16 we show the well measured cross section ^{197}Au(p,n)^{197}Hg. The activation, ground, and first isomer cross sections all peak near 10 MeV, the difference for the activation cross section is a factor of 1.4. Of note is the behavior of all three cross sections above 14 MeV, the experiments indicate a rapid decline, whereas the calculations are more gradual. We attribute this to the pre-equilibrium normalization more than the proton optical model.

4.1.6. Comparison to experimental (n,n') cross sections

In order to properly account for the population of the isomers via scattering we include (n,n') reactions that couple all isomer excited states specified in table A. Our calculations agree very well with with the measured (n,n') data from ground state to first isomer in Figure 21 (Appendix **??**). These are the only available data sets for odd-Z nuclei in the range of interest in this study , although our success with other isotopes from previous efforts ((Hoffman *et al.* 2004c), (Hoffman *et al.* 2008)) has been good.

Interestingly, the variation in the (n,n') cross sections shows virtually no sensitivity to the uncertainties in either the average radiative widths or level spacings. Indeed the only varition occurs for neutron energies $E_n \geq 10$ MeV. This is due to the variation we adopted for adjustment to the matrix elements affecting the amount of pre-equilibrium used in the calculation. The parameter in TALYS that adjusts this is **M2Constant**, with a default value of 1.0 for the choice of pre-equlibrium model we chose (an exciton model with analytical transition rates with an energy dependent matrix element **preeqmode**=1, the default in TALYS). Our variation was 0.75 and 1.25, giving a smaller or larger cross section, respectively. The range of potential values is 0. ≤**M2Constant** ≤ 100.

5. Conclusions

We have developed new neutron induced cross section detector sets for radiochemical diagnostics for thulium ($Z = 69$, $165 \leq A \leq 174$), lutetium ($Z = 71$, $170 \leq A \leq 179$), and tantelum ($Z = 73$, $178 \leq A \leq 185$). The theory and implementation of the Hauser-Feshbach model were described (§2), along with the details of the local systematics used to create a set of input parameters that

reflect the latest available experimental data in the local region of interest (§3). Modeled cross sections were compared to available experimental cross sections for the loaded detector elements, as well as other stable targets in the region. Sensitivity to reasonable variations in the parameters to the input models for the photon transmission coefficients, level densities, and pre-equilribrum was explored and presented in 4.1 and the Appendicies.

Overall we consider the modeling effort to be quite successful, as our calculated cross sections agree favorably with experimentally measured ones in this region of interest. In particular, we have demonstrated an ability to calculate (n,2n) cross sections to about 10% accuracy (Section 4.1.3), and (n,γ) cross sections to within roughly 15-20% accuracy, exceptions being the targets for lutetium and tantelum (Sections 4.1.1 and 4.1.2). Cross sections for reactions involving charged particles in the exit channel were shown to be very small compared to the dominant (n,2n), (n,3n), (n,n'), and (n,g) reactions that make up this set although our calculations did compare favorably to them (§ 4.1.5).

In our attempts to model cross sections it should be kept in mind that we are considering compound nuclear systems for which the important input parameters to our reaction model (e.g. those that affect level densities and photon-transmission coefficients) are often determined by normalization to experimental data (e.g. from resonance analysis), and so one would expect comparisons to measured capture cross sections to be good. Since these compound nuclei often bracket the systems of most interest to us, namely those which account for the dominant destruction reactions, our systematics should reasonably provide for similar agreement.

It is interesting that our neutron capture calculations which have experimental input for the most important quantities (average radiation widths and level spacings affecting the normalization of photon transmission coefficients and level densities) should fall short in specific regions (Lu, Ta) where they succeed in others (Tb, Ho, Tm, Re). Since all of these exhibit strong deformation (see figure 1), one might expect special development (coupled channels calculations) of the neutron transmission coefficient would address this shortcoming. But this is not the case for neutron capture reactions as can eb demonstrated by recalling the hauser feshbach formula, Eq. (1). In essence, transmission coefficients can be consideres as energy widths. Since photon widths are almost always smaller than particle widths the photon transmission coefficient can be neglected in the denominator of Eq. 1. Since charged particles reactions always have high thresholds due to the coulomb barrier, $\geq$ several MeV, these can also be neglected in the denominator, leaving only the neutron transmission coefficient, which essentially cancels out the same factor in the numerator of the Hauser Feshbach formula for this particluar channel. That leaves only the photon transmission coefficient (implicitly multiplied by the level density) as being the only quantities affecting neutron capture reactions Clearly something must be missing in our treatment of the nuclear level densities. As it stands, especially in this region, using global systematics for the average radiation widths, (n,γ) cross sections can typically be modeled within a factor of two, sometimes to within 30% (Hoffman *et al.* 1999).

This work was performed under the auspices of the U.S. Department of Energy by the University of California Lawrence Livermore National Laboratory in part under contract W-7405-ENG-48 and in part under Contract DE-AC52-07NA27344.

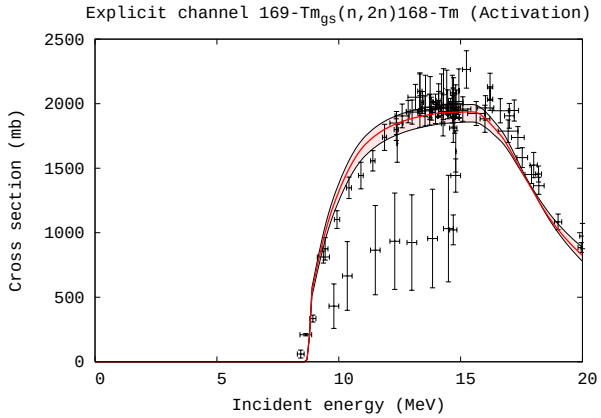

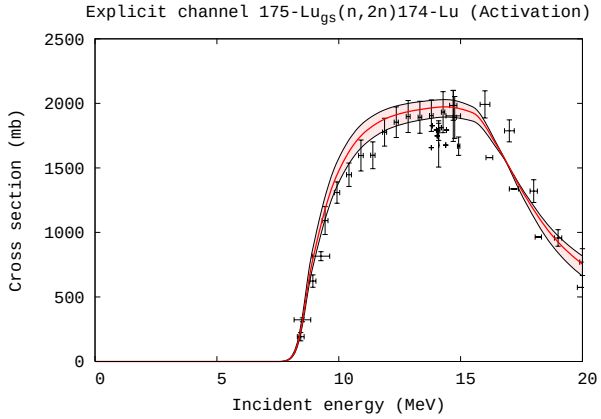

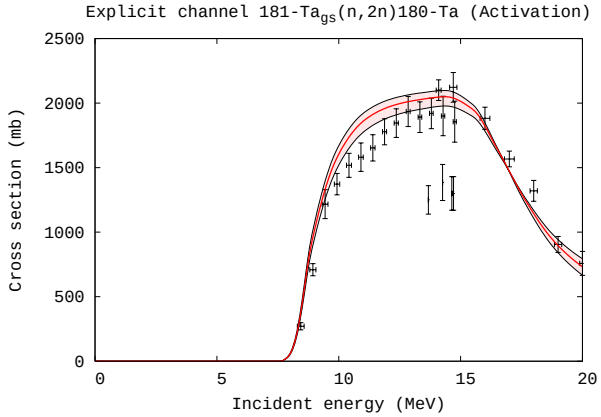

Fig. 13.— Calculated vs. measured (n,2n) cross sections on select stable isotopes in the region of interest. The data is taken from (EXFOR 2006). The red line represents the calculation using the central values of the average radiative width ($\langle\Gamma_\gamma\rangle_0$, Eq. 19) and the measured average level spacing (D_0), as well as the multiplier on pre-equlibrium (0.75 and 1.25). The black curves above and below filled with red represent the variation in the cross section when considereing the uncertainties on all these quantities (Figures 7 and 9).

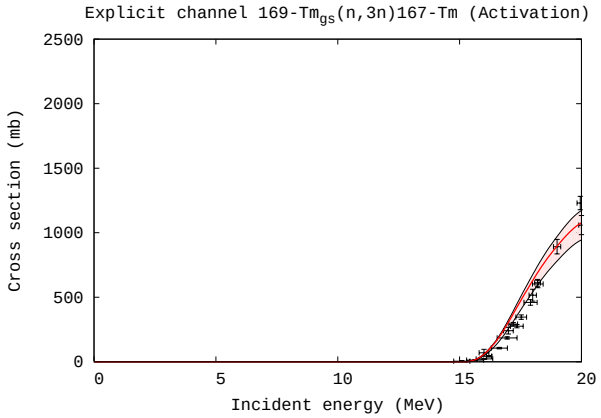

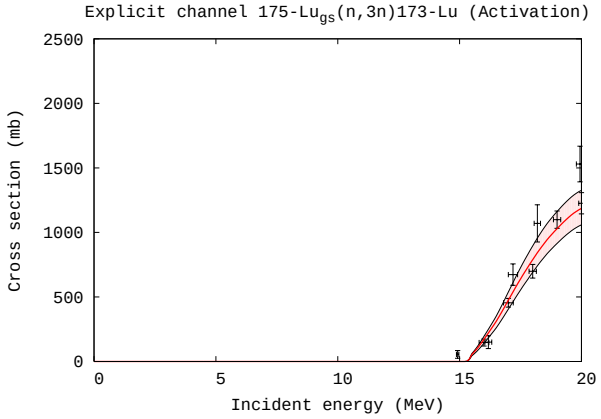

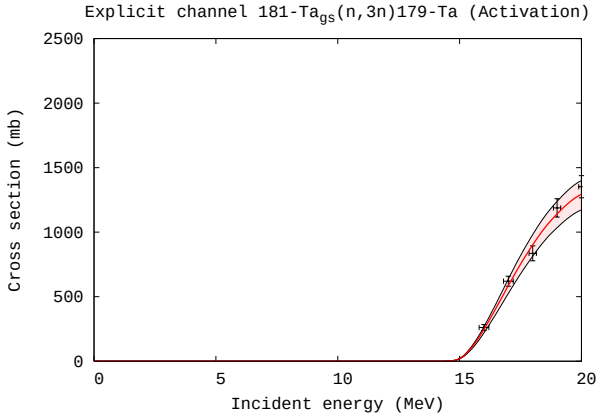

Fig. 14.— Calculated vs. measured (n,3n) cross sections on select stable isotopes in the region of interest. The data is taken from (EXFOR 2006). The red line represents the calculation using the central values of the average radiative width ($\langle\Gamma_\gamma\rangle_0$, Eq. 19) and the measured average level spacing (D_0), as well as the multiplier on pre-equlibrium (0.75 and 1.25). The black curves above and below filled with red represent the variation in the cross section when considereing the uncertainties on all these quantities (Figures 7 and 9).

REFERENCES

Gardener, M. A., & Howerton, R. J. "ACTL: Evaluated Neutron Activation Cross-Section Library" UCRL-50400, Vol. 18, version 2 (Oct. 1978)

Audi, G., Wapstra, A.H., and Thibault, C., "The AME2003 atomic mass evaluation (II). Tables, graphs, and references", Nuc. Phys. A **729**, 337 (2003).

Avrigeanu, V., Hodgson, P.E., and Avrigeanu, M., "Global optical potentials for emitted alpha particles", Phys. Rev. C **49**, 2136 (1994).

Avrigeanu, M. and Avrigeanu, V., "Recent improvements of the STAPRE-H95 pre-equilibrium and statistical model code", Report NP-86-1995, IPNE-Bucharest (1995). http://www.nea.fr/abs/html/iaea0971.html

Bao, Z. Y., Beer, H., Kappeler, F., Voss, F., & Wisshak, K., "Neutron cross sections for nucleosynthesis studies", Atomic Data & Nuclear Data Tables, **76**, 70 (2000). See also Karlsrhue Astrophysical Database of nucleosynthesis in Stars (KADONIS) http://www.kadonis.org/

Bauer, R., & Kelley, K. private communication (2007).

Beer, H., Voss, F., & Winters, R. R., "On the calculation of Maxwellian-averaged capture cross sections", ApJS, **80**, 403 (1992).

Belgya, T., Bersillon, O., Copote Noy, R., Fukahori, T., Zhigang, G., Goriely, S., Herman, M., Ignatyuk, A.V., Kailas, S., Koning, A.J., Oblozinsky, P., Plujko, V, and Young, P.G., "Handbook for calculations of nuclear reaction data, RIPL-2", IAEA, Vienna (2005).

Bohr, A., & Mottelson, B. *Nuclear Structure* Vol. 1, Single-Particle Motion, World Scientific, 1998

Chadwick, M., "The GNASH statistical model code", 1998. http://www.nea.fr/abs/html/psr-0125.html

Cline, C. K., "The Pauli exclusion principle in pre-equilibrium decay", Nucl. Phys. **A195**, 353 (1972).

Cline, C.K., and Blann, M., "The pre-equilibrium statistical model: description of the nuclear equilibration process and parameterization of the model", Nuc. Phys. A **172**, 225 (1971).

Dietrich, F.S., 2001, private communication.

Experimental Nuclear Reaction Data File, Brookhaven National Laboratory, US Dept. of Energy (2006). http://www.nndc.bnl.gov/exfor3/

Evaluated Nuclear Structure Data File, Brookhaven National Laboratory NNDC, US Dept. of Energy (2006). http://www.nndc.bnl.gov/ensdf/

Gardner, D.G., "Model calculations as one means of satisfying the neutron cross section requirements of the CTR program", Invited paper presented at the Conference on Nuclear Cross Sections and Technology, Washington, D.C., March 3-7, 1975.

Garrett, P. et. al. 1994 Nucl. Phys. **A568**, 445.

Garrett, P. et. al. 1994 Nucl. Phys. **A571**, 103.

Garrett, P. et. al. 1995 Nucl. Phys. **A581**, 267.

Garrett, P. et. al. 1996 Nucl. Phys. **A611**, 68.

Garrett, P. et. al. 2000 Nucl. Phys. **A662**, 235.

Gilbert, A. and Cameron, A.G.W., "A composite nuclear-level density formula with shell corrections", Can. J. Phys., **43**, 1446 (1965).

Hauser, W. and Feshbach, H., "The inelastic scattering of neutrons", Phys. Rev. **87**, 366 (1952).

Hilaire, S., Lagrange, Ch., and Koning, A. J., "Comparisons between various width fluctuation correction factors for compound nucleus reactions" Ann. of Phys. **306**, 209 (2003).

Hoffman, R. D., Rauscher, T., Woosley, S. E. & Thielemann, F.-K., "The reaction rate sensitivity of nucleosynthesis in Type II supernovae", ApJ, **521**, 735 (1999).

Hoffman, R.D., Dietrich, F.S., Bauer, R., Kelley, K., and Mustafa, M.G., "Neutron and charged-particle induced cross sections for radiochemistry in the region of bromine and krypton", UCRL-TR-205563, LLNL (2004a).

Hoffman, R.D., Dietrich, F.S., Bauer, R., Kelley, K., and Mustafa, M.G., "Neutron and charged-particle induced cross sections for radiochemistry in the region of iodine and xenon", UCRL-TR-206721, LLNL (2004b).

Hoffman, R.D., Kelley, K., Dietrich, F.S., Bauer, R., and Mustafa, M.G., "Neutron and charged-particle induced cross sections for radiochemistry in the region of samarium, europium and gadolinium", UCRL-TR-211558, LLNL (2004c).

Hoffman, R.D., Kelley, K., Dietrich, F.S., Bauer, R., and Mustafa, M.G., "Modeled neutron and charged-particle induced nuclear reaction cross sections for radiochemistry in the region of yttrium, zirconium, niobium, and molybdenum", UCRL-TR-222275, LLNL (2006c).

Hoffman, R.D., Dietrich, F.S., Kelley, K., Escher, J., Bauer, R., and Mustafa, M.G., "Modeled neutron and charged-particle induced nuclear reaction cross sections for radiochemistry in the region of iridium and gold", UCRL-TR-401969, LLNL (2008).

Hofmann, H.M., Richert, J., Tepel, J. W., and Weidenmu̇ller, H.A., "Direct reactions and Hauser-Feshbach theory" Ann. of Phys. **90**, 403 (1975).

Iljinov, A.S., Mebel, M.V., Bianchi, N., De Sanctis, E., Guaraldo, C., Lucherini, V., Muccifora, V., Polli, E., Reolon, A.R., and Rossi, P., "Phenomenological statistical analysis of level densities, decay widths and lifetimes of excited nuclei", Nucl. Phys. A **543**, 517 (1992).

Keisch, B., "Yield ratios of isomers produced by neutron activation", Phys. Rev. **129**, 769 (1963).

Kelley, K., Hoffman, R.D., Dietrich, F.S., Bauer, R., and Mustafa, M.G., "'Neutron and charged-particle induced cross sections for radiochemistry for isotopes of scandium, titanium, vanadium, chromium, manganese, and iron", UCRL-TR-211668, LLNL (2005).

Kelley, K., Hoffman, R.D., Dietrich, F.S., and Mustafa, M.G., "Neutron induced cross sections for radiochemistry for isotopes of arsenic", UCRL-TR-218181, LLNL (2006a).

Kelley, K., Hoffman, R.D., Dietrich, F.S., and Mustafa, M.G., "Neutron induced cross sections for radiochemistry for isotopes of nickel, copper, and zinc", UCRL-TR-221759, LLNL (2006b).

Kopecky, J. and Uhl, M., "Test of gamma-ray strength functions in nuclear reaction model calculations", Phys. Rev. C **41**, 1941 (1990).

Lohr, J.M. and Haeberli, W., "Elastic scattering of 9-13 MeV vector polarized deuterons", Nuc. Phys. A **232**, 381 (1974).

Mahaux, C. and Weidenmüller, H.A., "Recent developments in compound-nucleus theory", Ann. Rev. Part. Nucl. Sci. **29**, 1 (1979).

Milazzo-Colli, L., and Braga-Marcazzan, G.M., "α-emission by pre-equilibrium processes in (n,α) reactions", Nuc. Phys. A **210**, 297 (1973).

Moldauer, P. A., "Evaluation of the fluctuation enhancement factor" Phys. Rev. C **14**, 764 (1976).

Möller, P., Nix, J.R., Myers, W.D., and Swiatecki, W.J., "Nuclear ground-state masses and deformations" At. Data & Nuc. Data Tables **59**, 185 (1995).

Mughabghab, S.F., Divadeenam, M., and Holden, N.E., *Neutron Cross Sections*, Vols. 1 and 2, Academic Press (1981).

Nethaway, D.R., "The cross-section sets used with the Watusi program", A-Division memo, LLNL (5 Nov. 1998).

Rauscher, T., Thielemann, F.-K., and Kratz, K.-L., "Nuclear level density and the determination of thermonuclear rates for astrophysics", Phys. Rev. C **56**, 1613 (1997).

Raynal, J. "ECIS96", Proceedings of the Specialists' Meeting on the Nucleon Nucleus Optical Model up to 200 MeV, 13-15 November 1996, Bruyeres-le-Chatel, France. http://www.nea.fr/html/science/om200/raynal.pdf

Chadwick, M.B., Frankle, S., Trellue, H., Talou, P., Kawano, T., Young, P.G., MacFarlane, R.F., and Wilkerson, C. W., Nuclear Data Sheets, **108**, Number 12, 2716 (2007).

Koning, A., Hilaire, S.,& Goriely, S. "TALYS-1.4: A nuclear reaction program", Dec. 28, 2011 http://www.talys.eu/

Tuli, J.K., "Nuclear wallet cards", 6th Ed., Brookhaven National Laboratory, U.S. Dept. of Energy (2000).

Uhl, M., and Strohmaier, B., "STAPRE: A computer code for particle induced activation cross sections and related quantities", IRK-Vienna Report IRK-76/01 (1976, Upd. 1978).

Vonach, H., "User's manual for the code STAPRE as implemented at Lawrence Livermore National Laboratory", UCID-19549, LLNL (1982).

Wapstra, A.H., Audi, G., and Thibault, C., "The AME2003 atomic mass evaluation (I). Evaluation of input data, adjustment procedures", Nuc. Phys. A **729**, 129 (2003).

Williams, F.C. Jr., "Intermediate state transition rates in the Griffin model", Phys. Lett. **31B**, 184 (1970).

This 2-column preprint was prepared with the AAS LaTeX macros v5.0.

A. Cross Sections Included in the Detector Sets

Cross sections for (n,3n), (n,2n), (n,γ), and (n,n$'$) reactions on the targets listed below constitue the existing RADCHEM data sets Tm0193, Lu0284, and Ta0784. The new evaluation also includes (n,p) cross sections. Isomer spin assignments reflect modern values with parenthesis indicating an uncertain assigment. The majority of the reactions in Tm0193 and Lu0284 were calculated between 1984 and 1993. A few had been scaled to match measured cross sections at or around 14.1 MeV of incident energy.

A.1. Thulium, Lutetium, and Tantalum Detector Sets

Table 1:: Neutron induced reactions calculated for new Tm, Lu, and Ta sets

^{A}Z	lifetime	J^{π}	E_{mx} (MeV)	(n,3n)	(n,2n)	(n,n$'$)	(n,γ)	(n,p)
^{166}Tm	7.70 h	2+			○	○	○	○
^{167}Tm	9.25 d	1/2+			○	○	○	○
^{167}Tm$_{m1}$	1.16μs	7/2+	0.1796		○	○	○	○
^{168}Tm	93.1 d	3+		○	○	○	○	○
^{168}Tm$_{m1}$	0.76 ns	(1)-	0.0030	○	○	○	○	○
^{169}Tm	100%	1/2+		○	○	○	○	○
^{170}Tm	128.6 d	1-		○	○	○	○	○
^{170}Tm$_{m1}$	4.12 μs	(3)+	0.1832	○	○	○	○	○
^{171}Tm	1.92 y	1/2+		○	○	○	○	○
^{171}Tm$_{m1}$	2.60 μs	7/2-	0.4249	○	○	○	○	○
^{172}Tm	63.5 h	2-		○	○	○	○	○
^{173}Tm	8.24 h	(1/2+)		○	○	○	○	○
^{173}Tm$_{m1}$	10 μs	(7/2-)	0.3177	○	○	○	○	○
^{168}Lu	5.50 m	(6-)		○	○	○	○	○
^{168}Lu$_{m1}$	6.70 m	3+	0.2200	○	○	○	○	○
^{169}Lu	34.06 h	7/2+		○	○	○	○	○
^{169}Lu$_{m1}$	160 s	1/2-	0.2900	○	○	○	○	○
^{170}Lu	2.00 d	0+		○	○	○	○	○
^{170}Lu$_{m1}$	0.67 s	4-	0.0929	○	○	○	○	○
^{171}Lu	8.24 d	7/2+		○	○	○	○	○
^{171}Lu$_{m1}$	79.0 s	1/2-	0.0711	○	○	○	○	○
^{172}Lu	6.70 d	4-		○	○	○	○	○
^{172}Lu$_{m1}$	3.70 m	1-	0.0419	○	○	○	○	○
^{173}Lu	1.37 y	7/2+		○	○	○	○	○
^{173}Lu$_{m1}$	74.2 μs	5/2-	0.1237	○	○	○	○	○
^{174}Lu	3.31 y	(1)-		○	○	○	○	○
^{174}Lu$_{m1}$	142 d	(6)-	0.1708	○	○	○	○	○
^{175}Lu	97.41%	7/2+		○	○	○	○	○
^{175}Lu$_{m1}$	1.49 μs	5/2-	0.3533	○	○	○	○	○
^{176}Lu	2.59%	7-		○	○	○	○	○
^{176}Lu$_{m1}$	3.66 h	1-	0.1228	○	○	○	○	○
^{177}Lu	6.65 d	7/2+		○	○	○	○	○
^{177}Lu$_{m1}$	155 μs	1/2+	0.5697	○	○	○	○	○
^{177}Lu$_{m2}$	160.4 d	23/2-	0.9702	○	○	○	○	○
^{178}Lu	28.4 m	1(+)		○	○	○	○	○

A.2. Q-Values for Reactions Studied

Here we present the Q-values (in MeV) for each of the reactions included in this study. The values provided in this table are for reactions proceeding from the ground state of the target to the ground state of the residual. The Q-value for reactions proceeding from/to other states can be obtained by adding the energy of the target state to the given Q-value and subtracting the energy of the residual state. The values are calculated from our adopted mass excesses, as described in section 3.1.1. Inelastic scattering reactions such as (n,n') have thresholds equal to the energy of the first excited state. See the discrete level schemes (Appendix **??**).

Table 2:: Reaction Q-values

Target	$Q_{(n,\gamma)}$	$Q_{(n,2n)}$	$Q_{(n,3n)}$	$Q_{(n,p)}$	$Q_{(n,\alpha)}$
^{164}Tm	9.119	-7.225	-16.547	4.844	10.961
^{165}Tm	7.029	-9.119	-16.344	2.375	8.758
^{166}Tm	8.726	-7.029	-16.148	3.820	10.136
^{167}Tm	6.841	-8.726	-15.755	1.531	8.085
^{168}Tm	8.034	-6.841	-15.566	2.461	9.233
^{169}Tm	6.592	-8.034	-14.874	0.431	7.443
^{170}Tm	7.486	-6.592	-14.626	1.096	8.132
^{171}Tm	6.236	-7.486	-14.078	-0.708	6.498
^{172}Tm	6.950	-6.236	-13.722	-0.108	7.070
^{173}Tm	5.682	-6.950	-13.186	-1.822	5.632
^{174}Tm	6.517	-5.682	-12.632	-1.138	6.302
Target	$Q_{(n,\gamma)}$	$Q_{(n,2n)}$	$Q_{(n,3n)}$	$Q_{(n,p)}$	$Q_{(n,\alpha)}$
^{170}Lu	8.595	-7.304	-16.389	4.241	10.885
^{171}Lu	6.979	-8.595	-15.899	2.261	9.130
^{172}Lu	8.216	-6.979	-15.574	3.301	10.185
^{173}Lu	6.761	-8.216	-15.195	1.453	8.561
^{174}Lu	7.667	-6.761	-14.976	2.157	9.287
^{175}Lu	6.288	-7.667	-14.428	0.312	7.856
^{176}Lu	7.073	-6.288	-13.955	0.889	8.518
^{177}Lu	6.025	-7.073	-13.361	-0.617	7.127
^{178}Lu	6.792	-6.025	-13.098	0.138	7.619
^{179}Lu	5.693	-6.792	-12.818	-1.866	5.956
^{180}Lu	6.126	-5.693	-12.485	-1.499	6.430
Target	$Q_{(n,\gamma)}$	$Q_{(n,2n)}$	$Q_{(n,3n)}$	$Q_{(n,p)}$	$Q_{(n,\alpha)}$
^{178}Ta	7.930	-6.855	-15.285	2.719	10.310
^{179}Ta	6.641	-7.930	-14.785	0.888	8.667
^{180}Ta	7.577	-6.641	-14.572	1.635	9.099
^{181}Ta	6.063	-7.577	-14.218	-0.247	7.548
^{182}Ta	6.934	-6.063	-13.640	0.408	8.277
^{183}Ta	5.616	-6.934	-12.997	-1.228	7.036
^{184}Ta	6.626	-5.616	-12.551	-0.558	7.545
^{185}Ta	5.284	-6.626	-12.243	-2.255	6.130

A.3. Level Density Parameters

Here we present the level density parameters, as described in section 3.3, for each nucleus considered as a target, compound nucleus, or possible exit channel in this study. The first column lists the nuclei included. The second column is the asymptotic level density parameter $\tilde{a}$ in MeV^{-1}. Column three is the backshift Δ in MeV. Columns four and five are the shell correction δW in MeV and a flag that indicates whether $\tilde{a}$ is based on an experimentally measured resonance spacing (x) or is taken from systematics (s). Column six gives the matching energy E_x. Columns seven, eight, and nine are the constant temperature parameters: the squared spin cutoff parameter $\sigma(E_x)^2$, the nuclear temperature T, and E_0 (both in MeV) all evaluated at E_x. The last column indicates the number of excited states N to which the level density was fit, which is also the number of excited states included in our Hauser-Feshbach calculations.

Table 3: Level Density Parameters

Target	$\tilde{a}$	Δ	δW	x/s	E_x	$\sigma(E_x)^2$	T	E_0	N
^{159}Tb	16.214	0.952	2.902		4.370	8.250	0.520	-1.040	15
^{160}Tb	16.387	0.000	2.585	*	3.260	6.276	0.509	-1.763	22
^{165}Ho	17.064	0.934	2.065		4.942	7.518	0.562	-1.339	16
^{166}Ho	17.216	0.000	1.719	*	2.883	12.715	0.480	-1.242	16
^{165}Tm	17.064	0.934	2.978		4.560	8.739	0.519	-1.303	17
^{166}Tm	17.207	0.000	2.797		1.850	9.831	0.368	-0.666	1
^{167}Tm	17.349	0.929	2.434		4.751	8.895	0.537	-1.324	19
^{168}Tm	17.492	0.000	2.063		3.236	8.079	0.496	-1.625	16
^{169}Tm	17.634	0.923	2.010		4.728	10.024	0.537	-1.171	20
^{170}Tm	17.687	0.000	1.522	*	3.118	8.548	0.494	-1.375	21
^{171}Tm	18.125	0.918	1.646	*	4.457	11.134	0.515	-0.846	15
^{172}Tm	18.063	0.000	1.159		2.415	10.015	0.442	-0.800	13
^{173}Tm	18.207	0.912	1.459		3.009	10.738	0.407	0.253	17
^{174}Tm	20.864	0.000	1.183		3.690	10.075	0.490	-1.471	1
^{171}Lu	17.920	0.918	2.424		4.535	9.550	0.511	-1.161	15
^{172}Lu	18.063	0.000	2.110		3.247	5.280	0.486	-1.665	15
^{173}Lu	18.207	0.912	2.052		4.557	11.115	0.514	-1.077	19
^{174}Lu	18.350	0.000	1.595		2.663	10.278	0.447	-1.080	17
^{175}Lu	18.494	0.907	1.719		4.571	11.600	0.516	-0.990	16
^{176}Lu	18.382	0.000	1.384	*	3.006	14.188	0.477	-1.269	20
^{177}Lu	17.840	0.902	1.748	*	4.469	10.323	0.520	-0.878	20
^{178}Lu	18.925	0.000	1.334		1.777	19.298	0.374	-0.457	15
^{179}Lu	19.070	0.897	1.634		2.902	5.096	0.384	0.247	15
^{177}Ta	21.172	0.902	2.201		5.182	11.917	0.504	-1.080	17
^{178}Ta	18.925	0.000	1.842		2.158	10.195	0.393	-0.785	1
^{179}Ta	19.070	0.897	1.880		4.091	12.595	0.470	-0.685	19
^{180}Ta	19.214	0.000	1.387		2.552	15.714	0.431	-0.976	16
^{181}Ta	20.254	0.892	1.427	*	2.438	24.774	0.330	0.558	20
^{182}Ta	18.847	0.000	1.176	*	3.041	10.964	0.476	-1.238	17
^{183}Ta	18.747	0.887	1.518	*	3.556	7.883	0.443	-0.171	15

Continued on next page...

Table 3: (continued)

Target	$\tilde{a}$	Δ	δW	x/s	E_x	$\sigma(E_x)^2$	T	E_0	N
^{184}Ta	19.793	0.000	1.386		2.354	10.372	0.408	-0.855	6
^{185}Re	19.938	0.882	1.105		4.083	10.552	0.472	-0.495	18
^{186}Re	19.952	0.000	0.932	*	3.094	9.387	0.468	-1.245	26
^{187}Re	20.228	0.878	1.029		4.443	5.964	0.493	-0.745	21
^{188}Re	20.490	0.000	0.838	*	3.397	5.654	0.482	-1.444	20

B. Modeled Cross Sections Compared to Measurements

B.1. (n,γ)

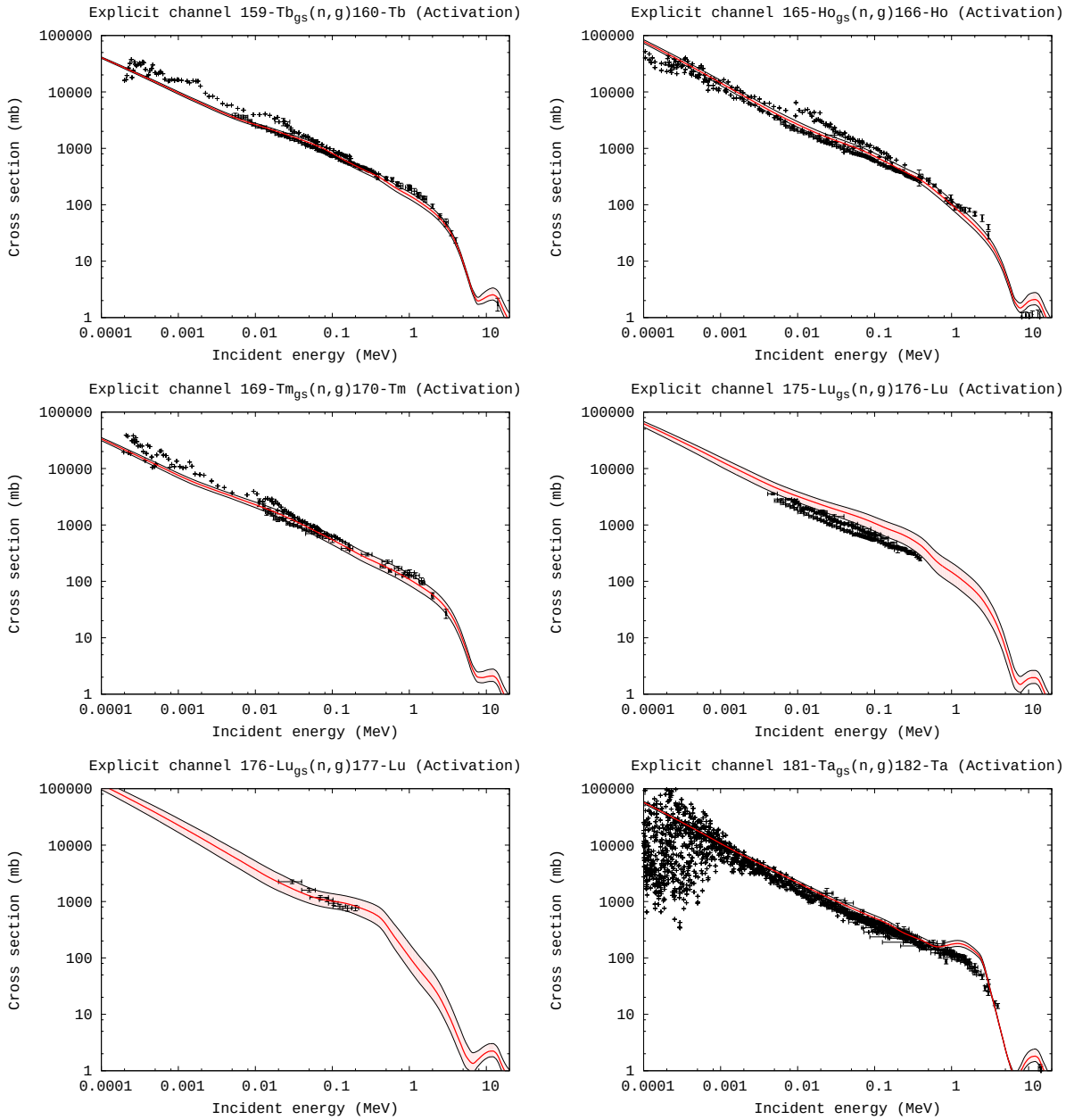

Fig. 15.— Modeled neutron capture cross sections compared to measurement. The red, and black solid lines represent our modeled cross sections assuming the central values of the average level spacing and radiative width ((Belgya *et al.* 2005)) and thier uncertainties. The data is taken from (EXFOR 2006).

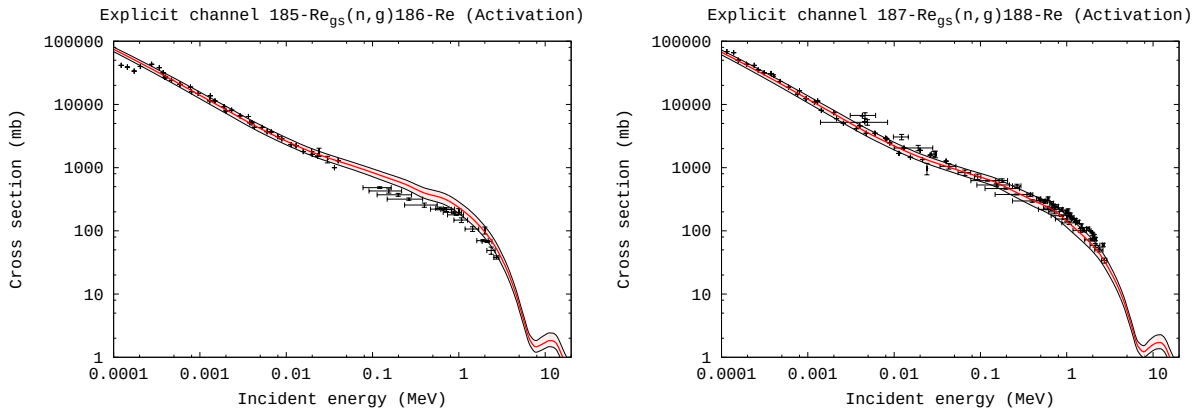

Fig. 16.— Modeled neutron capture cross sections compared to measurement. The red, and black solid lines represent our modeled cross sections assuming the central values of the average level spacing and radiative width ((Belgya *et al.* 2005)) and thier uncertainties. The data is taken from (EXFOR 2006).

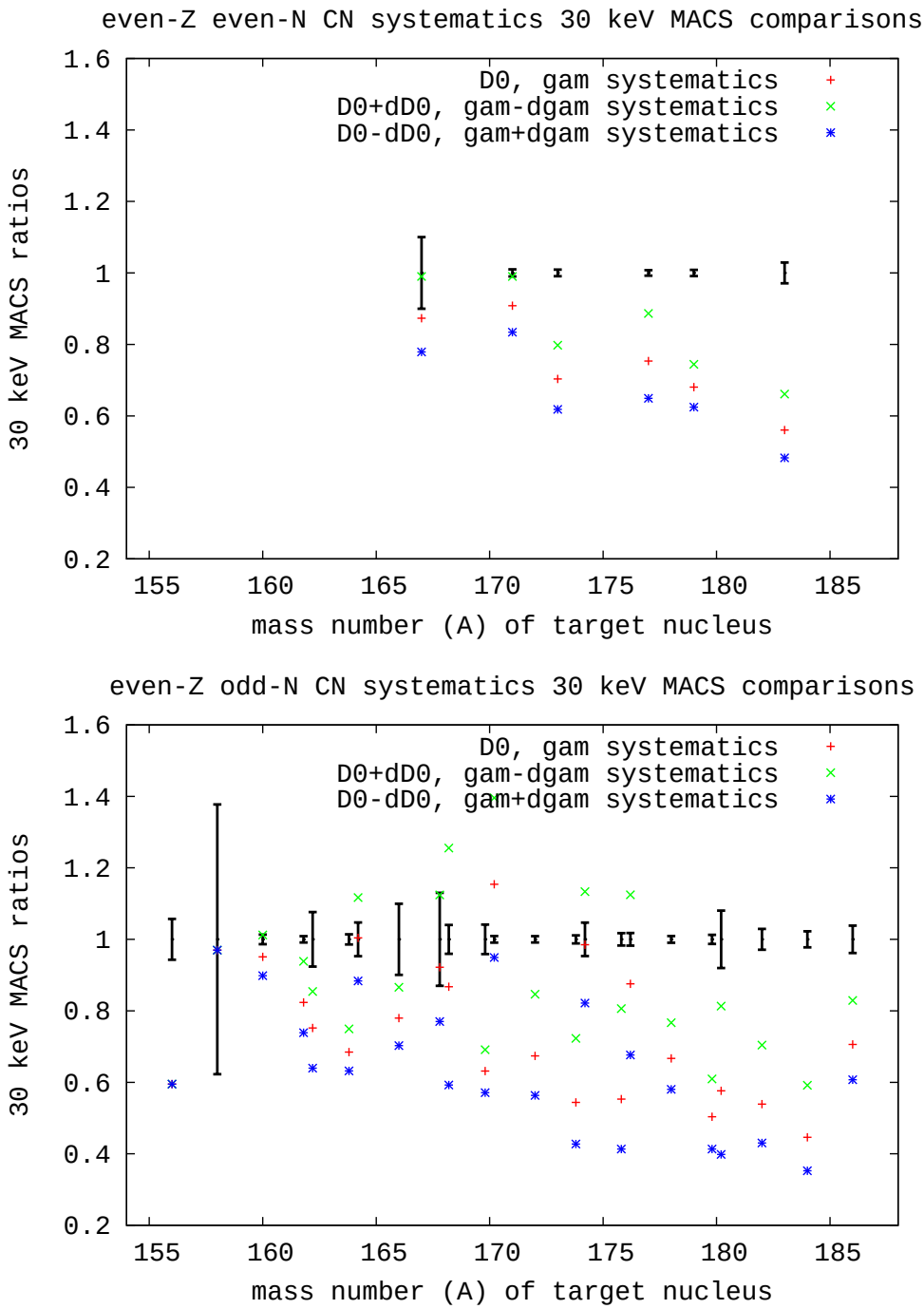

Fig. 17.— Modeled Maxwellian-averaged 30 keV capture cross sections compared to measurement. The data is taken from (Bao *et al.* 2000). The black solid lines represent the uncertainty associated with a evaluated 30 keV maxwellian averaged neutron capture cross section. MACS for a range of target nuclei are shown ($150 \leq A \leq 190$) for even-Z even-N compound nuclei (top panel) and even-Z odd-N compound nuclei (bottom panel). For each target the blue and green stars (either above, below, or straddling the measured MACS) represent the upper and lower limits, respectivley, of our calculated of the 30 keV MACS assuming the range of uncertainty in the average radiative width and level spacings shown in Figures 7 and 8.

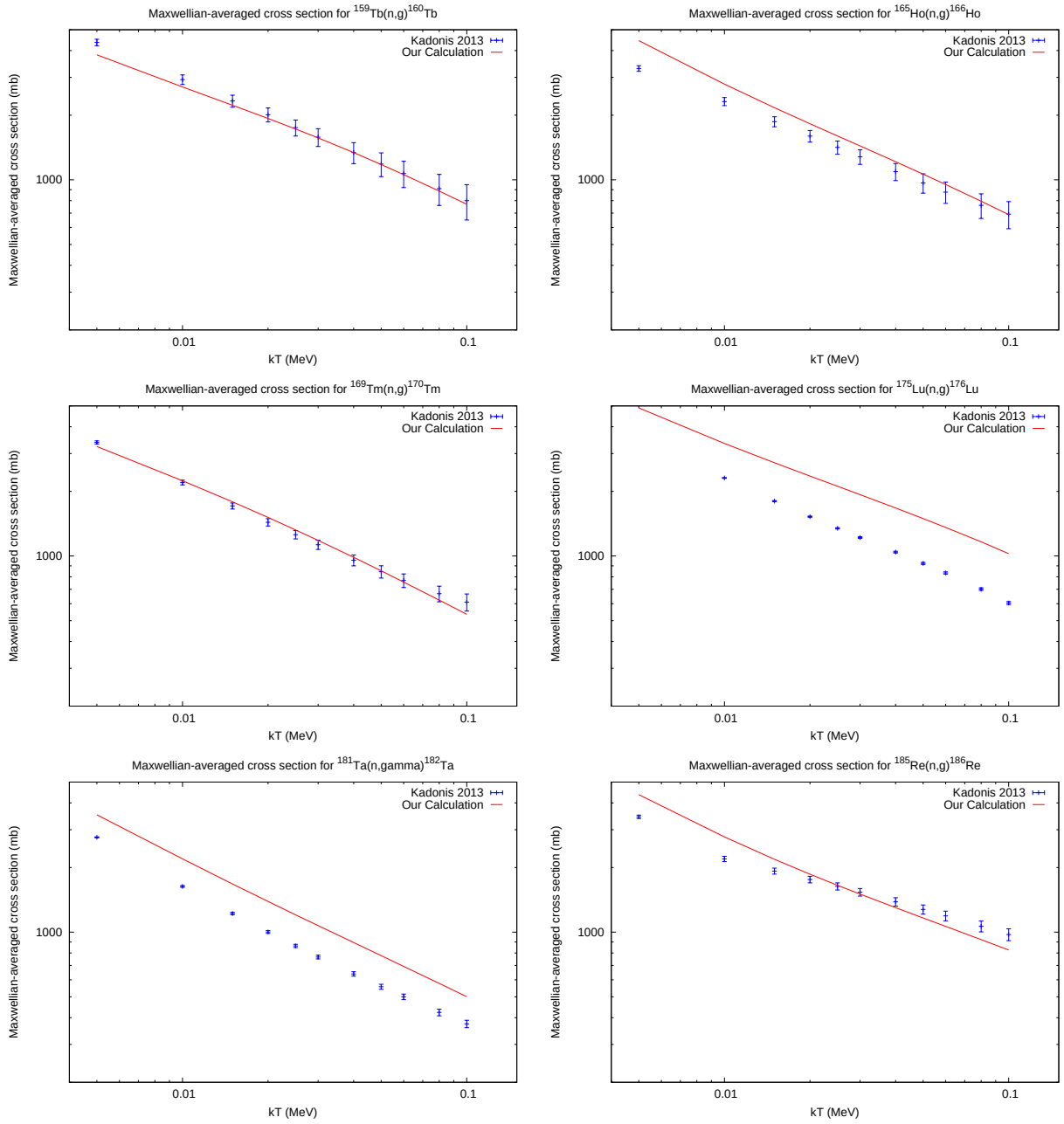

Fig. 18.— Calculated vs. recommended Maxwellian-averaged capture cross sections on odd-z stable targets The data is taken from (Bao *et al.* 2000). The solid line represent our modeled cross section. The data points are the recommended values, with the error bars for each energy identical to the quoted error at 30 keV.

B.2. (n,2n)

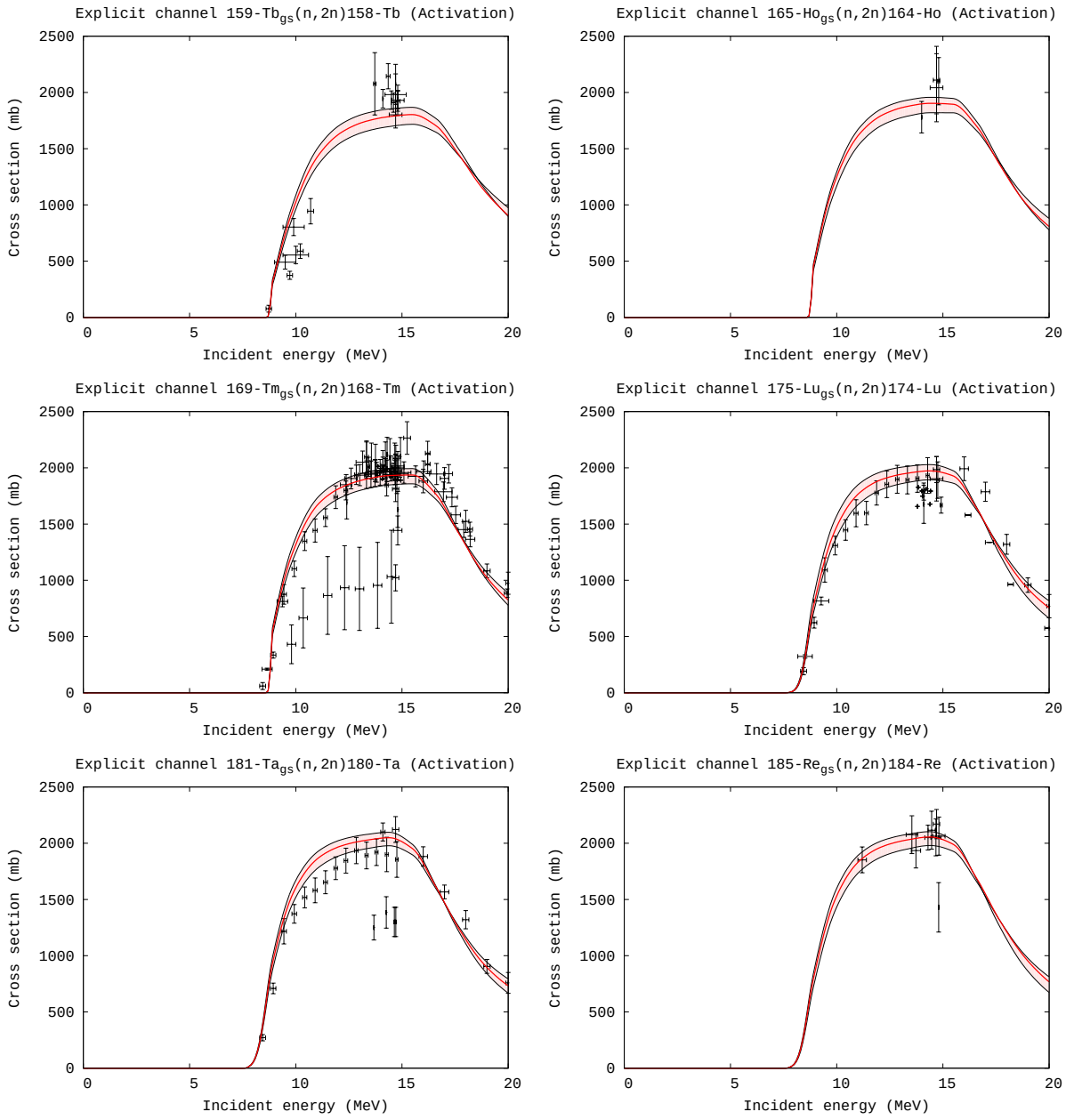

Fig. 19.— Modeled (n,2n) cross sections compared to measurement. The data is taken from (EXFOR 2006). The black, red, and blue solid lines represent our modeled cross sections (total, leading to the ground state, and leading to the first isomer, respectively). The Grey, orange, and light blue data points are measured cross section data (total, ground state, and first isomer).

B.3. (n,p)

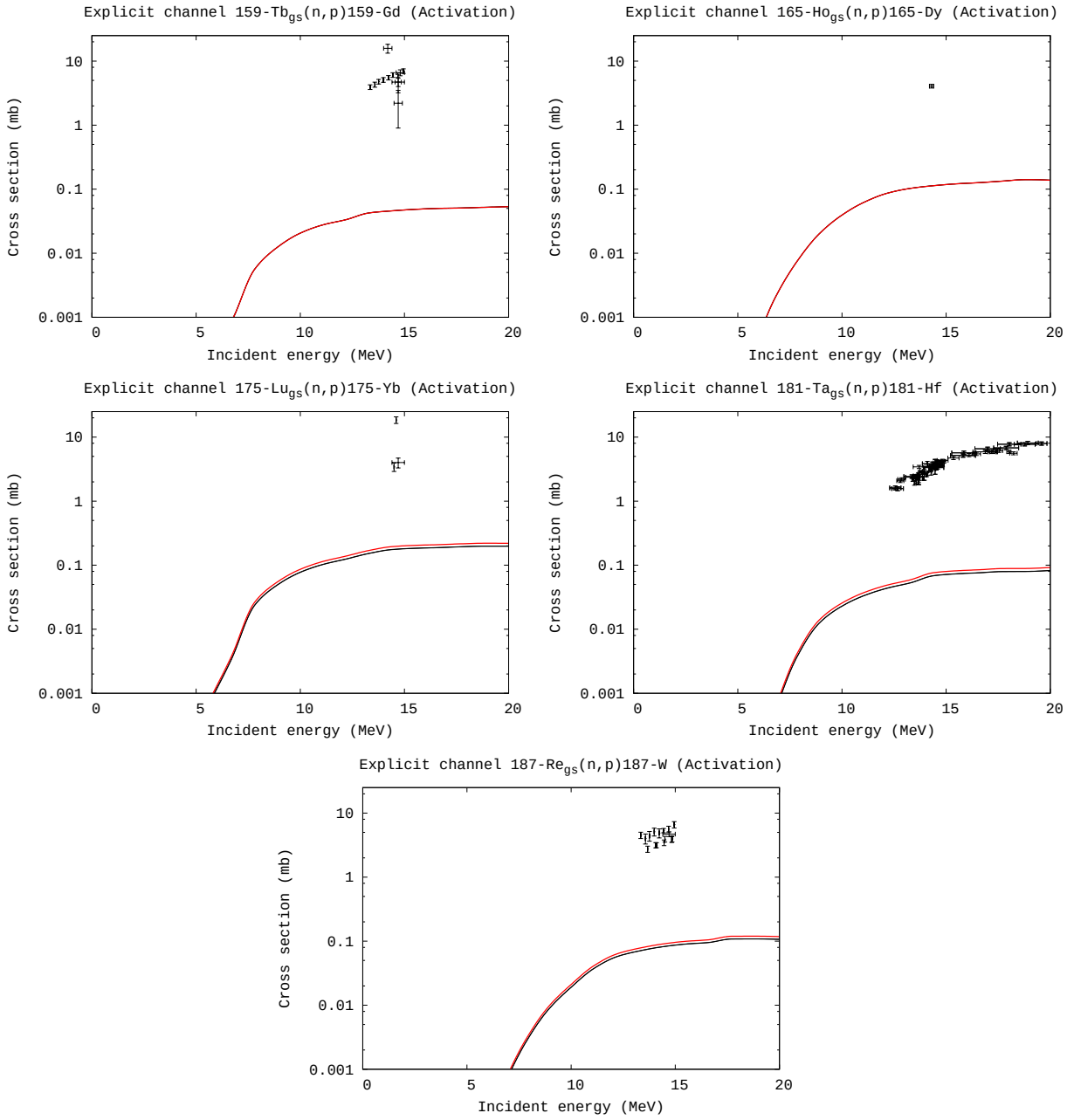

Fig. 20.— Modeled (n,p) cross sections compared to measurement. The red, and black solid lines represent our modeled cross sections assuming the central values of the average level spacing and radiative width ((Belgya *et al.* 2005)) and thier uncertainties. The data is taken from (EXFOR 2006).

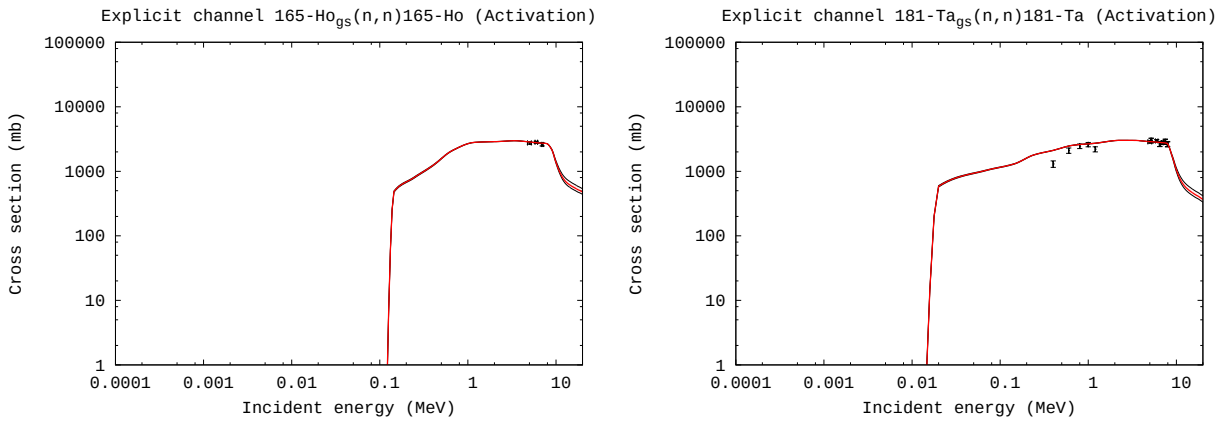

Fig. 21.— Calculated vs. measured (n,n') cross sections on select stable isotopes in the region of interest. The data is taken from (EXFOR 2006). The red line represents the calculation using the central values of the average radiative width ($\langle\Gamma_\gamma\rangle_0$, Eq. 19) and the measured average level spacing (D_0). The black curves above and below filled with red represent the variation in the cross section when considereing the uncertainties on both quantities (Figures 7 and 9).

B.4. (n,n)